THE FLUID-COUPLED MOTION OF MICRO AND NANOSCALE CANTILEVERS

BY

CARLOS CARVAJAL

A thesis submitted to the Faculty of the
Virginia Polytechnic Institute and State University
in Partial Fulfillment of the Requirements for the Degree of

MASTER OF SCIENCE
in
Mechanical Engineering

Mark R. Paul, Chair
Mark Stremler
Danesh Tafti

December 3, 2007
Blacksburg, Virginia

Keywords: Cantilevers, Fluid Coupled, Microscale, Nanoscale, Piezoshaker

Library Rights Statement

In presenting the thesis *The Fluid-Coupled Motion of Micro and Nanoscale Cantilevers* in partial fulfillment of the requirements for an advanced degree at Virginia Polytechnic Institute and State University, I agree that the Library shall make it freely available for inspection. I further agree that permission for copying as provided for by the Copyright Law of the U. S. (Title 17, U.S. Code) of this thesis for scholarly purpose may be granted by the Librarian. It is understood that any copying of publication of this thesis for financial gain shall not be allowed without my written permission.

I hereby grant permission to the VPI&SU Library to copy my thesis for scholarly purposes.

_____

Carlos Carvajal

_____

Date

Abstract

THE FLUID-COUPLED MOTION OF MICRO AND NANOSCALE CANTILEVERS

BY

CARLOS CARVAJAL

An understanding of the fluid coupled dynamics of micro and nanotechnology has the potential to yield significant advances yet many open and interesting questions remain. As an important example we consider the coupling of two closely spaced cantilevers immersed in a viscous fluid subject to an external driving. While one cantilever is driven to oscillate, the adjacent cantilever is passive. This system is modeled as two simple harmonic oscillators in an array whose motion is coupled through the fluid. Using simplified geometries and the unsteady Stokes equations, an analytical expression is developed that describes the dynamics of the passive cantilever. Full numerical simulations of the fluid-solid interactions that include the precise geometries of interest are performed. The analytical expressions are compared with the numerical simulations to develop insight into the fluid-coupled dynamics over a range of experimentally relevant parameters including the cantilever separation and frequency based Reynolds number. In addition, a shaker-based actuation device is investigated in order to demonstrate its feasibility for use with micro and nanoscale systems.

Acknowledgements

I want to first thank my savior, Jesus Christ, who has blessed me and given me the knowledge and strength to succeed through this journey in my life. I would like to thank my mom, grandmother, brother and sister for their support and encouragement through the hard times. Also, I want to acknowledge my loving fiancée, Cayci, not only for her support, but for her continuous love and encouragement. I want to send out a special thank you to my advisor, Dr. Mark R. Paul, who has not only been a great mentor, but also a friend. Dr. Paul is a remarkable advisor and I gratefully thank him for his guidance, encouragement and useful discussions in the midst of this work. I would like to thank my committee members, Dr. Mark Stremler and Dr. Danesh Tafti for their contribution to this work. Finally, I want to acknowledge my labmates, classmates and friends for their help and encouragement.

Table of Contents

List of Figures

List of Tables

Nomenclature

L	Cantilever length, (m)
w	Cantilever width, (m)
h	Cantilever height, (m)
a	Cylinder radius (m)
A_0	Amplitude of oscillation, (m)
ω_d	Driving frequency of oscillation, (rad/s)
ω_f	Resonant frequency in fluid, (rad/s)
k	Spring stiffness constant, (N/m)
E_c	Young's modulus, (N/m^2)
ρ_c	Solid density, (kg/m^3)
ρ_f	Fluid density, (kg/m^3)
μ	Dynamic viscosity (kg/m s)
ν	Kinematic viscosity μ/ρ_f, (m^2/s)
Kn	Knudsen number
λ	Mean free path, (m)
L_c	Characteristic length scale, (m)
$\vec{u}$	Velocity vector, (m/s)
t	Time, (s)
p	Pressure, (N/m^2)

U_o	Maximum velocity, (m/s)
R_u	Velocity based Reynolds number
R_ω	Frequency based Reynolds number
ψ	Stream function, (m^3/s)
U_r	Radial velocity, (m/s)
U_θ	Theta velocity, (m/s)
θ	Angle, (rad)
K_1	Modified Bessel function
K_1'	First derivative of the modified Bessel function
F_f	Fluid force, (N)
M'	Mass of fluid displaced by a cylinder, (kg)
Δx	Spatial resolution, (m)
Δx_{max}	Maximum spatial-resolution, (m)
Δt	Time-step, (s)
Δt_{max}	Maximum time-step, (s)
T	Period of oscillation $2\pi/\omega$, (s)
E	Average absolute error, (%)
E_{max}	Maximum average absolute error, (%)
N	Integer number of data points
$x(t)$	Displacement of cantilever, (m)
$\dot{x}(t), \ddot{x}(t)$	Time derivatives of displacement (i.e. velocity and acceleration, respectively)

$y(t)$	Displacement of piezoshaker, (m)
Q	Quality factor
γ	Viscous damping, (N s/m)
γ'	Mass normalized viscous damping, (N s/kg m)
ω_n	Natural frequency, (rad/s)
$\widetilde{\omega}$	Nondimensional frequency
$\Gamma(R_\omega)$	Hydrodynamic function
$\Gamma_r(R_\omega)$	Real part of the hydrodynamic function
$\Gamma_i(R_\omega)$	Imaginary part of the hydrodynamic function
T_0	Mass loading parameter
φ	Phase of oscillation, (rad)
δ_s	Stokes length, (m)

1 General Overview

The dynamics of an array of cantilevers in fluid can be exploited to make measurements with unprecedented sensitivities. Studying the dynamics of single molecules in their natural environment is one exciting possibility. In order to accomplish such a possibility, it is important to first understand the fluid-coupled dynamics of an array of cantilevers, which will benefit both biological and medical applications. As a result, new knowledge about these interactions needs to be developed.

To increase our understanding of the fluid-coupled dynamics of an array of cantilevers, an analytical expression is developed to predict the amplitude and phase of a fluid-coupled cantilever. The case of interest is an array of two cantilevers immersed in a viscous fluid separated by a known distance. One cantilever is driven to oscillate causing the surrounding fluid to move. The moving fluid then causes the neighboring cantilever to oscillate. Using both analytics and finite element numerical simulations we build an understanding of the fluid-coupled dynamics. The work presented here is summarized below.

1. *Modeling the behavior of a single driven cantilever*. The first part of this thesis considers a single cantilever immersed in a stationary, unbounded fluid. The cantilever is driven to oscillate sinusoidally. An analytical solution to the unsteady Stokes equations is used to provide a basic understanding of the fluid dynamics and the force that is exerted on the cantilever.

2. *The fluid coupling between a single cantilever and a piezoshaker*. We study the dynamics of a single cantilever immersed in fluid that is driven to oscillate by placing the cantilever and liquid on a piezoshaker. We determine the usefulness and efficiency of a piezoshaker device when the elastic objects are micro and nanoscale.

3. *Analytical modeling of an array of cantilevers in fluid.* We study the dynamics of an array of two cantilevers immersed in a fluid. One cantilever is driven externally and the adjacent cantilever oscillates because of the resulting fluid motion. An analytical expression is developed to predict the amplitude and phase of the fluid-coupled cantilever.

4. *A numerical investigation of an array of cantilevers in fluid.* We have performed finite element numerical simulations for the precise geometries of interest to validate our analytical predictions. The numerical simulations solve the complete fluid and solid equations and include the resulting fluid-solid interactions.

The overall contribution of this work is that we have shown that the piezoshaker method is promising for the actuation of micro scale systems that are immersed in a viscous fluid. Also, we have provided an analytical expression that describes the fluid-coupled dynamics of an array of cantilevers immersed in a viscous fluid, where one cantilever is driven externally and the adjacent cantilever oscillates because of the resulting fluid motion. The analytical expressions are validated using finite element numerical simulations for the precise geometries of interest and are anticipated to be of broad interest.

2 Introduction

Richard Feynman's famous talk "There is plenty of room at the bottom" in the 1960's encouraged people to explore the interesting and challenging world at small scales where new and exciting phenomena can be discovered (1) (2). In order to have a better understanding of the length scales under study: a human hair has a diameter of about 0.1 mm, and a nanotube has a diameter of about 1nm $(1\text{nm} = 1 \times 10^{-9}\text{m})$. This implies that 10 billion nanotubes can be placed up against a single human hair. Other examples of objects of various length scales are illustrated in Figure 1.

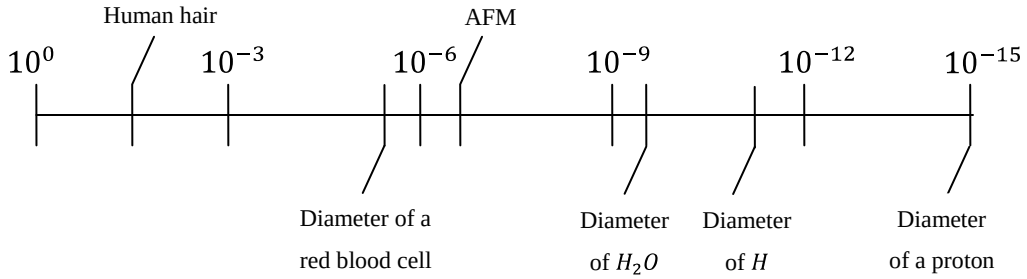

Figure 1 - Some illustrative examples of objects over a large range of length scales (shown in meters).

Technologies at the micro and nanoscales are known as Micro-Elecromechanical Systems (MEMS) and Nano-Electromechanical Systems (NEMS). These systems are still in their infancy. As technology improves and smaller devices are created the complexity of these devices increases. Having a basic understanding of the physics describing these systems is necessary for the new technology being developed.

In the last few decades, several methods have been developed to study single molecules. The Atomic Force Microscope (AFM) invented by Binnig, Quate, and Gerber in 1986 is capable of imaging, measuring, and manipulating matter with atomic precision (3). An important component of the AFM is an oscillating cantilever. Cantilevers are commonly fabricated

from silicon (Si), silicon nitride (SiN), or polymer (4). A weakness of the AFM is that it sometimes causes damage to samples. Methods utilized to displace the cantilever include: thermoelastic, magnetomotive, optical interferometric, and piezoelectric actuation.

In thermoelastic actuation, a gold layer is attached to the top of the beam which is heated by means of local Joule heating causing elastic expansion (5) (6). Magnetomotive actuation is a method where a doubly-clamped beam is placed in a uniform magnetic field and by applying a current to the beam, a driving force is generated causing the beam to displace (7). Optical interferometric actuation uses an amplitude-modulated driving diode laser to drive the beam and a continuous wave detection laser to read out the data (8) (9). A challenge that the optical interferometric method faces is the difficulty in aligning the laser as well as accessing dimensions far below the diffraction limit (10).

Lastly, the piezoshaker method uses a cantilever which is mounted onto a piezoelectric ceramic actuator disk (11) (12). The disk is excited by an input voltage causing the cantilever to displace. Current research shows that this method can be extended into the nanoscale (11). The piezoshaker method not only eliminates difficulties such as laser alignment, but is capable of accessing dimensions far below the diffraction limit. Also, the piezoshaker is a much simpler method for instrumentation design.

An array of cantilevers operating simultaneously will lead to more powerful, faster, and efficient technologies. An advantage is the ability to make multiple measurements simultaneously and to process the information in real time.

Cantilever arrays can be used as biosensors for medical diagnostic applications. Such applications include: protein detection, DNA hybridization, and drug discovery. Monitoring physiological parameters simultaneously and in real time like protein biomarkers can save lives. Experiments have demonstrated the ability to measure multiple label-free proteins by means of a cantilever beam array sensor in real-time (13). Another application is DNA

hybridization. DNA hybridization quantifies the efficiency and speed of two single strands of DNA to reassociate and form a double-stranded DNA. DNA hybridization is a fundamental application for studying the biological process of replication, transcription, and translation (14) (15).

Examples of cantilever arrays can also be observed in nature such as cilia and a gecko's setae. In the human lung cilia are little hairs that act like tiny brooms to push the bacteria from the lungs out into the throat, preventing illness. It is fascinating the way cilia work together in a cooperative matter to protect the human body. Gecko's setae are adhesive foot hairs which allow geckos to climb on vertical surfaces. A single toe can support the entire body weight. An example of an array of setae is shown in Figure 2.

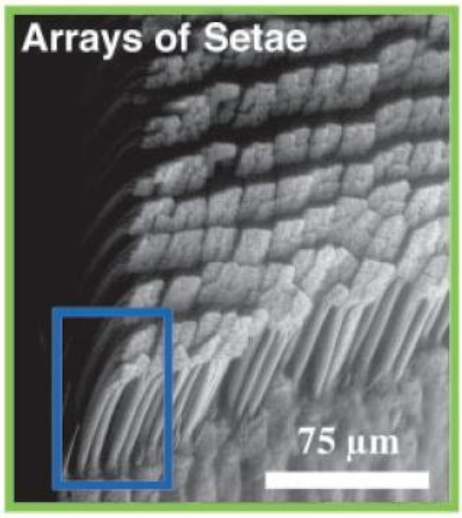

Figure 2 - A micrograph of the setae of a gecko. In the box on the lower left individual setae are visible (image reprint from ref. (16)).

Previous work includes the study of the hydrodynamic interaction between two micron sized beads immersed in fluid which were held at varying distances in optical traps. The bead displacements were then measured to quantify the Brownian dynamics (17). The study showed that the cross-correlations of the bead positions have time delayed anticorrelations.

Furthermore, it provides a framework for modeling the dynamics of microscopic biological systems such as proteins, organelles, and even cells.

The coupled motion of two micron sized beads immersed in fluid which were tethered together by an extended piece of DNA was also considered (18). This was done by using femtonewton force spectroscopy (FFS) to measure the thermal fluctuations of different DNA molecules at different extensions. FFS is a technique that allows the study of molecules and chemical bonds. This study showed unequal physical properties along the longitudinal and transverse axis of the DNA molecule, which may reveal exciting new physics.

The dynamics of single micro-cantilevers oscillating in fluid has been considered (19) (20) (21). This has been examined analytically and numerically by solving the incompressible Navier-Stokes equations coupled to the beam equation. The numerical calculations were conducted using fully finite element-based fluid structure interaction model. Results have shown that the force acting on the micro beam is a combination of viscous dissipation and an added mass effect, which corresponds to the mass of the cantilever and the mass of the fluid. The dissipation arises from localized fluid shear near the edges of the vibrating micro-cantilever. Furthermore, it is shown that existing two-dimensional analytical models tend to over predict the added mass effect (21).

The hydrodynamic coupling between micro-cantilevers which are driven coherently with the same frequency oscillating in viscous fluid has been investigated (22) . The unsteady Stokes equations are solved using a boundary integral technique. This study shows that the hydrodynamic coupling depends on the following parameters: the Reynolds number, separation between the beams, and the relative phase between the two microbeams. This implies that the hydrodynamic coupling between micro-cantilevers can be controlled by these parameters in a collective manner in order to minimize or maximize the loading on individual microbeams.

The stochastic dynamics of micron and nanoscale oscillators immersed in a viscous fluid has been studied (23)(24). The dynamics are dominated by the thermal bombardment of fluid molecules by Brownian motion. A thermodynamic approach based on the fluctuation-dissipation theorem is applied in order to quantify the stochastic dynamics of closely spaced micron and nanoscale objects. Results suggest that one can improve force resolution using correlated measurements. These results will help the design of future micro and nanoscale technologies that utilize thermal fluctuations.

The Brownian motion of a pair of silica particles trapped by a pair of laser traps was studied in order to measure the viscoelastic properties of the fluid (25). The cross-correlations of the particles displacement were used to analyze the experimental data. It was shown that the trapping causes anticorrelations in the motion of the two particles at low frequencies, which depends on trap strength and the shear modulus of the viscoelastic media.

3 Analytical solution for an oscillating cantilever in fluid

Determining the fluid-coupled dynamics of an array of micro-scale cantilevers is challenging. In order to understand the fluid-coupled dynamics, it is appropriate to first study the dynamics of a single cantilever in fluid.

3.1 Flow field

Consider a long slender cantilever ($L \gg w, h$) that is fixed at the base and free at the tip as shown in Figure 3. The cantilever is driven externally such that the time dependent displacement of the cantilever tip is given by

$$x_1(t) = A_0 \sin(\omega_d t) \tag{1}$$

where A_0 is the amplitude and ω_d is the driving frequency.

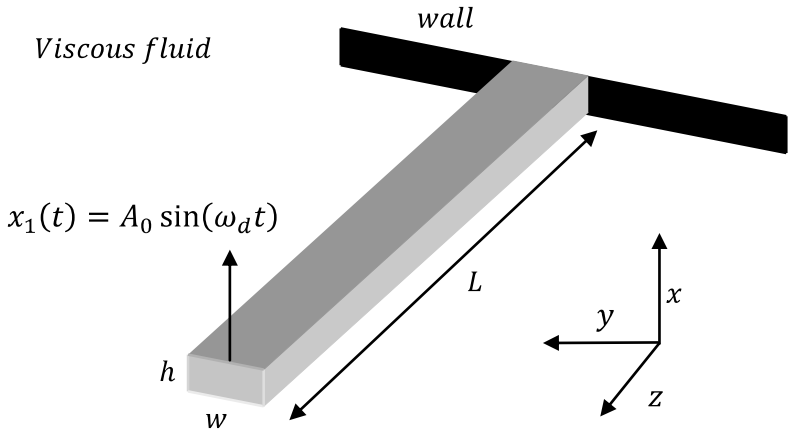

Figure 3 - A cantilever of length *L*, width *w*, and height *h* immersed in a viscous fluid. The cantilever is driven with a displacement given by $x_1(t)$.

The properties of the beam used here are summarized in Table 1 (this is the C2 cantilever of Ref. (26)).

Table 1 - The beam geometry: length *L*, width *w*, thickness *h*. The resonant frequency in fluid ω and spring constant *k*. The beam is made of silicon with Young's modulus E_c = 1.74 $\times 10^{11}$ N / m^2, and density ρ_c = 2320 kg / m^3. The fluid is water with density ρ_f = 997 kg / m^3, and dynamic viscosity μ = 8.59 $\times$ 10^{-4} kg / m s.

L	w	h	ω	k
197 μm	29 μm	2 μm	158.5 $\times 10^3$ $rad\ s^{-1}$	1.3 $N\ m^{-1}$

For long and slender beams most of the fluid flows around the sides. Overall, the flow over the cantilever tip has little effect on the dynamics. We assume that the cantilever is infinite in length and study a two dimensional cross section (20). We approximate the rectangular cross section of the cantilever to be cylindrical with a radius given by $w/2$ (19) (20). Tuck demonstrated that the hydrodynamic functions for a circular cylinder and an infinitely thin rectangular beam are approximately identical. The difference between the two never exceeds 15% over the range of four orders of magnitude of the frequency based Reynolds number.

We will use cylindrical coordinates (r, θ, z), where r is the radial coordinate, θ is the angular coordinate, and z is the axial coordinate. The cylinder radius $a = w/2$ and is shown in Figure 4.

It is worthwhile to briefly justify the use of continuum hydrodynamics. The assumption can be discussed using the Knudsen number $Kn = \lambda/L_c$, where λ is the mean free path of a molecule between collisions and L_c is a characteristic length scale. For $Kn \to 0$ the continuum hypothesis is valid because the mean free path between the molecules is much smaller than the characteristic length scale. Furthermore, comparison between experiment

and theory has shown that for values $Kn \lesssim 10^{-3}$ the fluid can be treated as a continuum without introducing significant error (27). The mean free path in a liquid is approximately the diameter of a single molecule. For water $\lambda \approx 0.3nm$ and if we take L_c to be the cylinder radius $a = 14.5\ \mu m$ this yields $Kn \approx 10^{-5} \ll 1$ and the continuum assumption is valid.

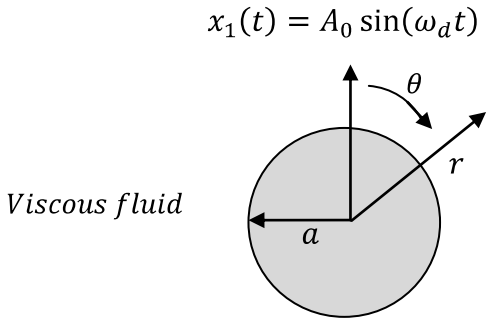

Figure 4 - An infinite cylinder of radius a oscillating in a viscous fluid with a prescribed displacement $x_1(t)$. The coordinate r is measured from the center of the cylinder and θ is the clockwise angle measured with respect to the vertical.

The equations governing the fluid motion are the incompressible Navier-Stokes equations

$$\rho_f \left(\frac{\partial \vec{u}}{\partial t} + \vec{u} \cdot \vec{\nabla}\vec{u}\right) = -\vec{\nabla}p + \mu \nabla^2 \vec{u}, \tag{2}$$

$$\vec{\nabla} \cdot \vec{u} = 0. \tag{3}$$

Where $\vec{u}$ is the fluid velocity, p is the pressure, ρ_f is the fluid density, t is time, and μ is the dynamic viscosity. Eq. (2) represents the conservation of momentum (where the body forces have been neglected). Eq. (3) represents the conservation of mass for an incompressible fluid.

Using L_c, ω_f^{-1}, U_0, and $\mu\, U_0/L_c$ as the characteristic length, time, velocity and pressure (a viscous based pressure) scales the nondimensional equations are

$$R_\omega \frac{\partial \vec{u}}{\partial t} + R_u \vec{u} \cdot \vec{\nabla}\vec{u} = -\vec{\nabla}p + \nabla^2 \vec{u} \tag{4}$$

$$\vec{\nabla} \cdot \vec{u} = 0 \tag{5}$$

where R_u and R_ω are the velocity and frequency based Reynolds numbers, respectively. The velocity based Reynolds number is given by

$$R_u = \frac{U_o L_c}{\nu} = \frac{A_0 \omega_f a}{\nu} \tag{6}$$

where ν is the kinematic viscosity. R_u is a ratio of convective inertial forces to viscous forces. Since both the characteristic length and the velocity scales are small, it implies that the system is viscosity dominated. This means the nonlinear convective inertia term $\vec{u} \cdot \vec{\nabla}\vec{u}$ becomes negligible when $R_u \ll 1$. Setting the characteristic length scale equal the radius of the cylinder $L_c = a = w/2$, and the characteristic velocity scale as $U_0 = A\omega_f$ (where we have chosen $A = a/100$ to represent the small deflections characteristic of these systems) yields $R_u = 0.38 < 1$. Therefore the nonlinear term will make a small contribution.

The frequency based Reynolds number is given by

$$R_\omega = \frac{\omega_f a^2}{\nu} \tag{7}$$

which is the ratio of local inertial acceleration forces to viscous forces. For the case of interest here $R_\omega = 38 \gg 1$. This indicates that the local inertial term $\partial\vec{u}/\partial t$ in Eq. (4) is significant, making the analysis more difficult. The simplified equations become

$$R_\omega \frac{\partial \vec{u}}{\partial t} = -\vec{\nabla} p + \nabla^2 \vec{u} \tag{8}$$

$$\vec{\nabla} \cdot \vec{u} = 0 \tag{9}$$

which are the unsteady Stokes equations. The analytical solution for the flow field was given by Stokes in 1850 (28). The details of this derivation are given in Appendix A. The solution to Eq. (8) and Eq. (9) are

$$u_r(r,t,\theta) = \frac{1}{r}\left(\frac{A}{r} + B\sqrt{iR_\omega}K_1\left[\frac{r}{a}\sqrt{iR_\omega}\right]\right)e^{i\omega t}\cos\theta \tag{10}$$

$$u_\theta(r,t,\theta) = \left(\frac{A}{r^2} - \frac{B}{a}\sqrt{iR_\omega}K_1'\left[\frac{r}{a}\sqrt{iR_\omega}\right]\right)e^{i\omega t}\sin\theta \tag{11}$$

where $i = \sqrt{-1}$, K_1 is the modified Bessel function of the second kind, and K_1' is the derivative of K_1. u_r and u_θ are the radial and angular flow field velocities, respectively.

A slice of interest of the flow field is at $\theta = \pi/2$ (see Figure 4), where the velocity in the radial direction $u_r = 0$. This is relevant to the study of the fluid-coupling of cantilevers when they are separated by a distance s along the $\theta = \pi/2$ axis (illustrated in Figure 11). u_θ is complex and the real and imaginary parts represent a phase shift of $\pi/2$ in time. The case of sinusoidally driven displacement corresponds to the real part of the complex velocity field. The imaginary part would correspond to a cosine driven displacement.

Near the oscillating cylinder a viscous layer develops called the Stokes layer. The Stokes layer δ_s describes the distance from the oscillating cylinder over which the bulk of the fluid momentum is able to diffuse. The Stoke layer is given by $\delta_s \sim \sqrt{\nu/\omega_f}$, or

$$\frac{\delta_s}{a} \sim {R_\omega}^{-1/2} . \tag{12}$$

For the case of interest here (shown in Table 1) ${R_\omega}^{-1/2} = 0.2$.

To have a better understanding of the flow field, $u_\theta(r,t)$ is evaluated for a single period of oscillation, $T = 2\pi/\omega_f$, at times T/4, T/2, 3T/4, and T as shown in Figure 5.

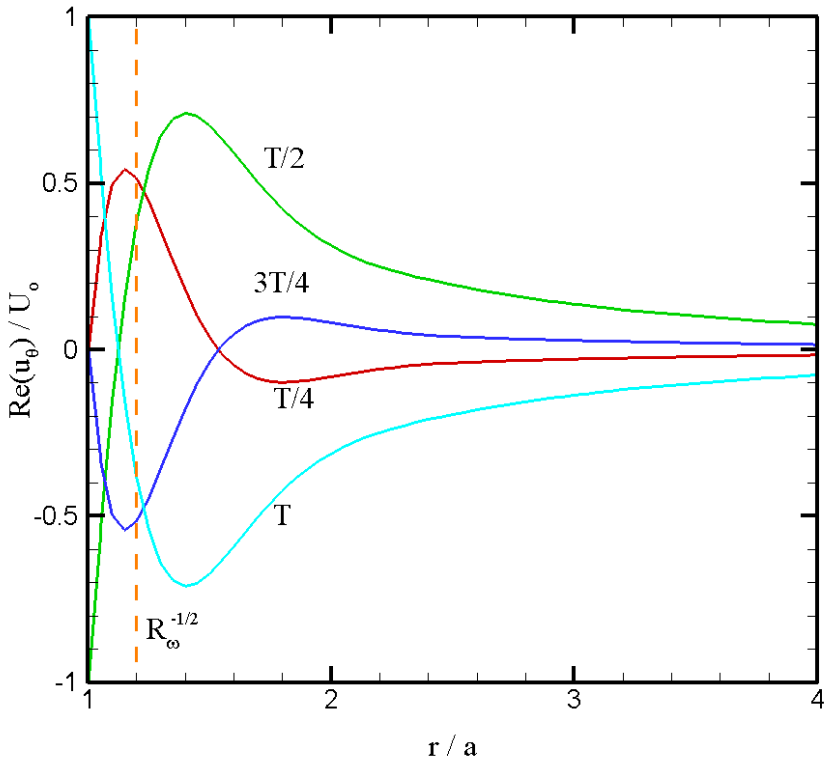

Figure 5 - The flow field caused by an infinite cylinder with radius *a* oscillating in fluid. (Dashed Line) Normalized Stokes layer with radius *a*. (Left axis) Normalized real part of the flow field velocity with the maximum velocity U_0. (Bottom axis) Normalized radial distance.

Figure 5 shows waves of momentum propagating in the radial direction and dissipating as time increases. The flow field is different when the cylinder is moving up (i.e. for time T) or down (i.e. for time T/2). It is clear that in the radial distance of $R_\omega{}^{-1/2}$ the flow is in the viscous regime as expected.

An additional diagnostic of interest is the quality factor Q. The quality factor is the ratio of the energy stored in a simple harmonic oscillator to the dissipated energy for a single oscillation. When Q is high, the system has little energy dissipation. When Q is low, the

system has significant energy dissipation. The expression of Q for an infinite cylinder is given by (20)

$$Q \approx \frac{\omega_f m_f}{\gamma_f} = \frac{\frac{1}{T_0}+\Gamma_r(R_\omega)}{\Gamma_i(R_\omega)} \tag{13}$$

where $\Gamma_r(R_\omega)$ and $\Gamma_i(R_\omega)$ are the real and imaginary parts of the hydrodynamic function $\Gamma(R_\omega)$ that is given by

$$\Gamma(R_\omega) = 1 - \frac{4K_1\sqrt{i\,R_\omega}}{K_1\sqrt{i\,R_\omega}+\sqrt{iR_\omega}K_1'\sqrt{i\,R_\omega}}. \tag{14}$$

The hydrodynamic function is a complex function. The real part denotes the added mass, which corresponds to the mass of the cylinder and the mass of the fluid m_f (29). m_f is given by

$$m_f = \alpha m_c(1 + T_0\Gamma_r(R_\omega)) \tag{15}$$

where m_c is the actual cantilever mass and for the fundamental mode of oscillation for a beam $\alpha = 0.243$. The constant T_0 is the mass loading parameter (29), which is the ratio of the mass of a cylinder of fluid with radius $a = w/2$ to the actual mass of the cantilever, given by

$$T_0 = \frac{m_{cyl}}{m_c} = \frac{\pi}{4}\frac{\rho_f}{\rho_c} \tag{16}$$

The imaginary part denotes the viscous damping γ_f (29), given by

$$\gamma_f = \alpha m_{cyl}\omega\Gamma_i(R_\omega). \tag{17}$$

3.2 The force acting on an oscillating cylinder in fluid

The force acting on an oscillating cylinder in fluid is derived in detail in Appendix B following the work of Stokes (28). The final expression is

$$F_f = -M' U_0 e^{i\omega t} i\omega \Gamma(R_\omega) = \gamma_f U_0 e^{i\omega t} \tag{18}$$

where $M' = \pi a^2 \rho_f$ is the mass per unit length of the fluid displaced by the cylinder and $\Gamma(R_\omega)$ is the hydrodynamic function given in Eq. (14). F_f can also be expressed as a damping force that is proportional to the relative velocity $U_0 e^{i\omega t}$ and the viscous damping $\gamma_f = -M' i\omega \Gamma(R_\omega)$.

4 The fluid coupled motion of a single cantilever and a piezoshaker

The piezoshaker method is an attractive method of actuation. For micro a nanoscale systems R_ω is small implying that the system is dominated by viscous forces. Determining how low of a Reynolds number it is still possible to see any significant oscillation of the beam is important for the usage of this method. This is of importance to our experimental collaborators because it is a readily available actuation mode for use with their current generation of NEMS devices. We emphasize that the rest of this thesis is valid for any actuation method and that this chapter stands alone as a study of one particularly interesting actuation mechanism.

Consider a cantilever with mass m and spring constant k that is immersed in a viscous fluid and placed on a piezoelectric actuator. Figure 6 illustrates a piezoshaker where the displacement of the cantilever and the displacement of the actuator are represented by $x(t)$ and $y(t)$, respectively.

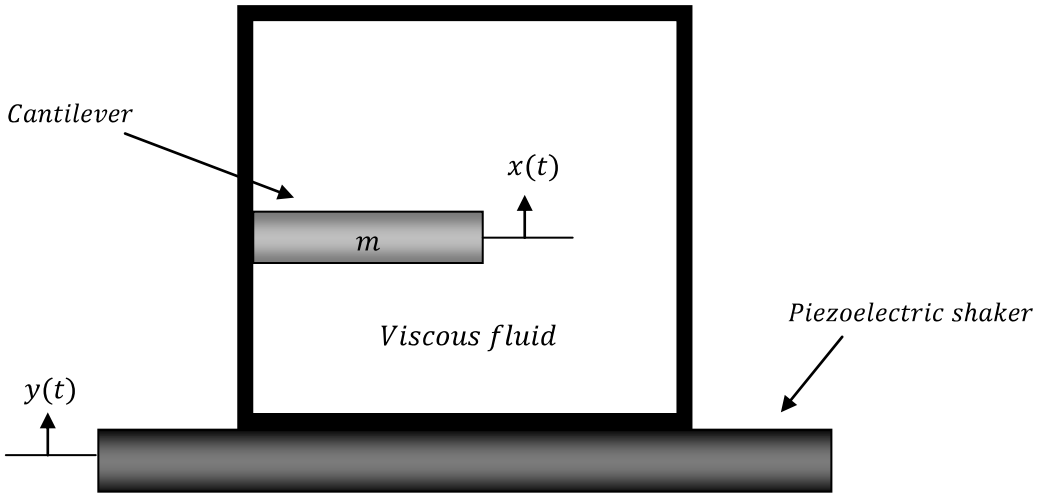

Figure 6 - A cantilever of mass *m* and spring constant *k* immersed in a viscous fluid. The beam is excited by a piezoelectric shaker which has a prescribed harmonic displacement *y*(*t*). The displacement of the cantilever is given by *x*(*t*).

Again we consider the flow over a two dimensional cross section of the beam which is modeled as a cylinder (20) and is shown in Figure 7.

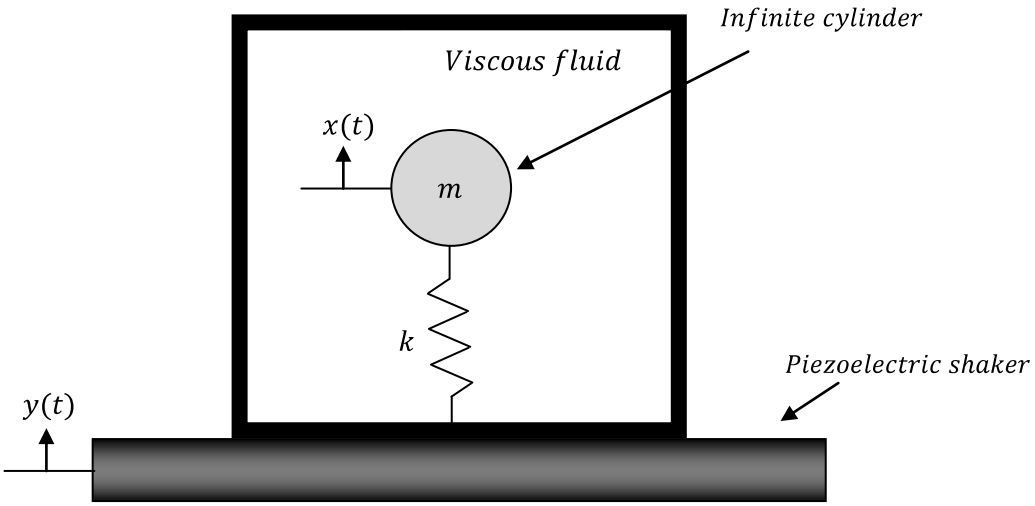

Figure 7 - An infinite cylinder of mass per unit length *m* with spring constant *k* immersed in a viscous fluid. The cylinder is excited by a piezoelectric shaker which has a prescribed harmonic displacement *y*(*t*). The displacement of the cylinder is given by $x(t)$.

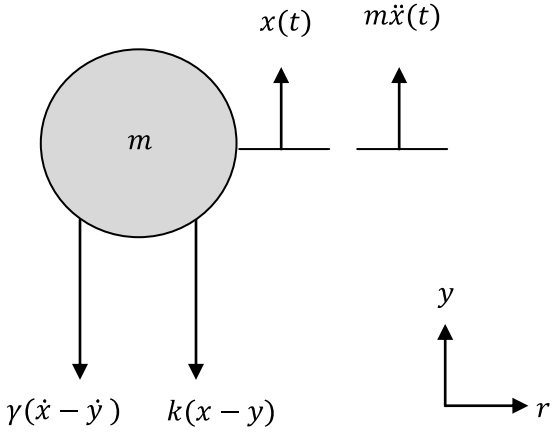

Figure 8 - Free body diagram of the forces acting on the mass *m*.

The forces acting on the mass m are shown in Figure 8, where the viscous fluid damping is denoted by γ. The governing equation of motion is given by:

$$m\,\ddot{x} + \gamma\,(\dot{x} - \dot{y}) + \,k\,(x - y) = 0 \tag{19}$$

where the piezoshaker displacement is given by,

$$y(t) = A\sin\,(\omega_d\,t) \tag{20}$$

where A is the amplitude of the piezoshaker and ω_d is the driving frequency. Substituting $y(t)$ in Eq. (19) yields,

$$m\,\ddot{x} + \gamma\dot{x} + \,kx = \gamma A\omega_d\cos(\omega_d t) + kA\sin(\omega_d t) \tag{21}$$

Eq. (21) is a linear second-order ordinary differential equation with solution (30)

$$\frac{x(t)}{A} = \omega_n\left[\frac{{\omega_n}^2+(2\zeta\omega_d)^2}{({\omega_n}^2-{\omega_d}^2)^2+(2\zeta\omega_d\omega_n)^2}\right]^{1/2}\cos(\omega_d t - \theta_1 - \theta_2) \tag{22}$$

where

$$\theta_1 = \tan^{-1}\frac{2\zeta\omega_n\omega_d}{{\omega_n}^2 - {\omega_d}^2}$$

$$\theta_2 = \tan^{-1}\frac{\omega_n}{2\zeta\omega_d}$$

and the natural frequency is ${\omega_n}^2 = k/m$. Noting that

$$2\zeta = \frac{\gamma}{m\omega_n} = \frac{1}{Q} \tag{23}$$

yields

$$\frac{x(t)}{A} = \left[\frac{1+\left(\frac{\tilde{\omega}}{Q}\right)^2}{(1-\tilde{\omega}^{\,2})^2+\left(\frac{\tilde{\omega}}{Q}\right)^2}\right]^{1/2}\cos(\omega_b t - \theta_1 - \theta_2) \tag{24}$$

where,

$$\theta_1 = \tan^{-1} \frac{1}{Q} \frac{\widetilde{\omega}}{(1-\widetilde{\omega}^2)}$$

$$\theta_2 = \tan^{-1} \frac{Q}{\widetilde{\omega}}$$

and $\widetilde{\omega} = \omega_d/\omega_n$. When the cylinder is driven at its resonant frequency $\widetilde{\omega} = 1$. Assuming that both the shaker and the cylinder are in phase; Eq. (24) simplifies to,

$$\frac{x}{A} = [\, Q^2 + 1 \,]^{1/2}. \tag{25}$$

Eq. (25) represents the maximum displacement of a simple harmonic oscillator with respect to the maximum amplitude of the shaker A. Note that for any given Q, this equation yields x/A. When Q = 0 (i.e. R_ω = 0), $x = A$, implying that both the cantilever and the shaker are moving as a solid body. In order to understand if the cantilever has any significant displacement relative to the piezoshaker, the normalized displacement of the cantilever is shown in Figure 9.

Since some micron and nanoscale systems of interest have spherical geometries (17) (18). It is interesting to include Q for a sphere of radius a,

$$Q = \frac{m\omega}{\gamma} = \frac{8}{9} R_\omega \tag{26}$$

where the Stokes drag law for a sphere is given by $\gamma = 6\pi\mu a$.

Figure 9 shows that the piezoshaker method is promising. For a better perspective of the usefulness and the efficiency of the piezoshaker method for the systems of interest, a microscale cantilever (the C2 cantilever (26)), and a nanoscale cantilever (29) were used as representative examples in Figure 10. R_ω for these devices are given in Table 2.

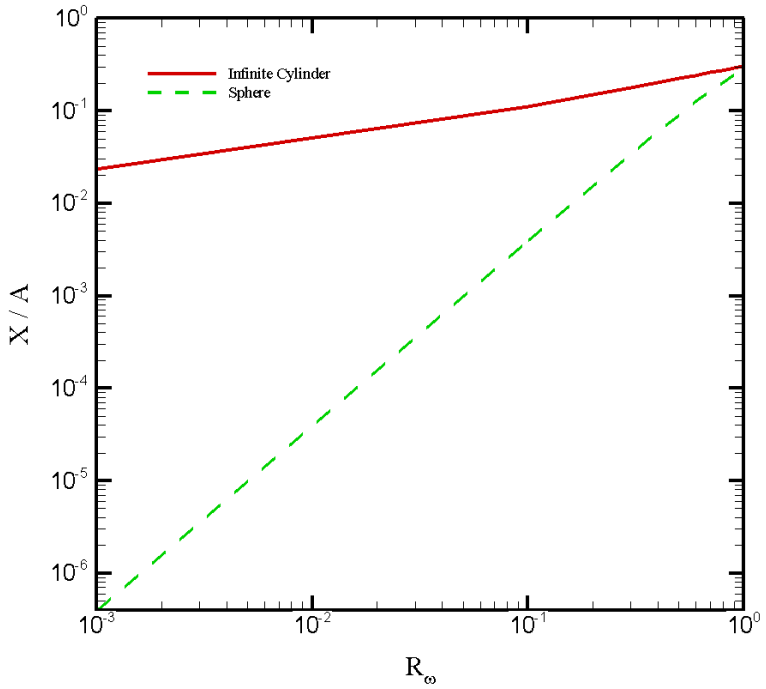

Figure 9 - Normalized displacement of an infinite cylinder and a sphere immersed in a viscous fluid utilizing a piezoshaker as the actuation method; (Solid Line) infinite cylinder; (Dashed Line) sphere. (Left axis) Normalized displacement of the cantilever beam with the maximum amplitude of the shaker *A*.

Table 2 - Frequency based Reynolds number R_ω for a microscale cantilever (the C2 cantilever) and a nanoscale cantilever.

	Microscale cantilever	Nanoscale cantilever
R_ω	38.7	0.026

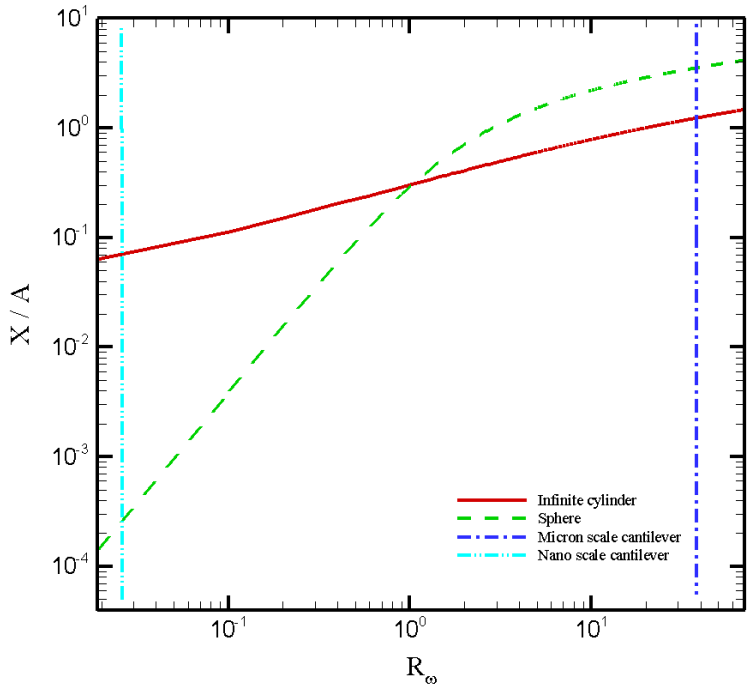

Figure 10 - The maximum amplitude of oscillation of an infinite cylinder and a sphere using the piezoshaker method with water as the working fluid: (Solid Line) infinite cylinder; (Dashed Line) sphere. (DashedDotDot Line) Representation of a nanoscale cantilever. (DashedDot Line) Representation of the microscale cantilever. (Left axis) Normalized displacement of the cantilever beam with the maximum amplitude *A* of the shaker.

Figure 10 shows that for the nanoscale cantilever the displacement is approximately a tenth of the actuators displacement. Likewise, for a nanoscale spherical geometry, the displacement is ten-thousandths of the actuators, implying that the piezoshaker method is not suitable for nanoscale systems. However, for the micron cantilever of interest, the displacement is slightly greater than the piezoshaker. Similarly, for micron scale spherical geometries the displacement is greater than the piezoshaker. It can be shown that for the system of $R_\omega \gtrsim 10$, a system will have a greater displacement than the piezoshaker because the damping acting on the system is small and the system is oscillating at its resonance

frequency. As a result, the piezoshaker method is promising for the actuation of micro scale systems that are immersed in fluid.

5 The fluid-coupled dynamics of an array of two cantilevers

We now study the fluid-coupled dynamics of an array of two micro-scale cantilevers immersed in fluid. We will develop an analytical expression that governs the dynamics of the fluid-coupled cantilever. The expression determines the amplitude and phase of the fluid-coupled cantilever.

Consider two cantilevers immersed in fluid that are separated by a distance s, illustrated in Figure 11. The driven cantilever on the left has a displacement given by

$$x_1(t) = A_{0_1} \sin(\omega_d t) \tag{27}$$

where A_{0_1} represents the amplitude of oscillation. The beam motion causes the fluid to move which causes the right cantilever beam to move.

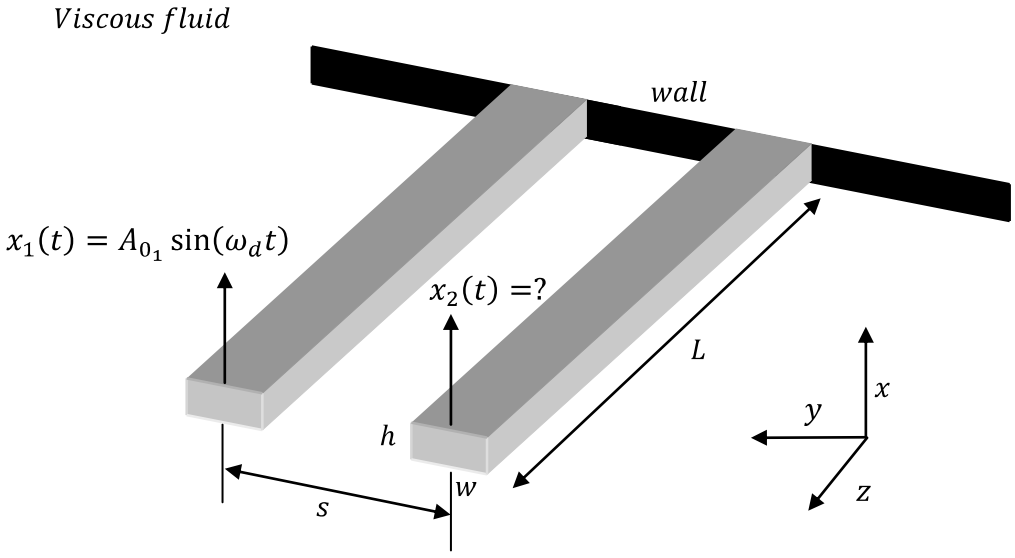

Figure 11 - An array of two cantilevers of length *L*, width *w*, and height *h* that are separated by a distance *s*, which are immersed in a viscous fluid. The left cantilever has a displacement given by $x_1(t)$. The right cantilever beam has a displacement represented by $x_2(t)$, which is being moved by the fluid motion caused by the left cantilever.

As before, the cantilevers are modeled as infinite cylinders as shown in Figure 12.

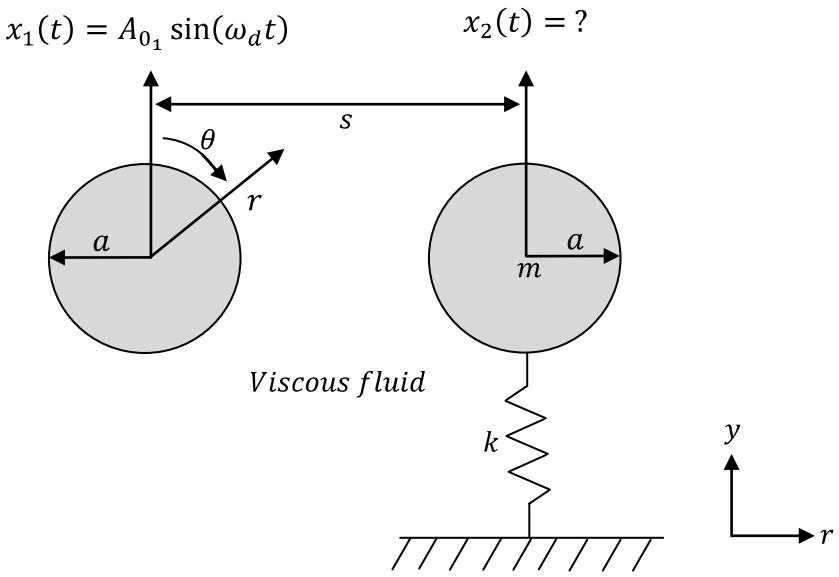

Figure 12 - An array of two infinite cylinders of radius *a*, separated by a distance *s* which are immersed in a viscous fluid. The left cylinder has a prescribed displacement given by $x_1(t)$. The right cylinder of mass *m* has a displacement $x_2(t)$ caused by the fluid motion. The right cylinder has a spring constant *k*.

A free body diagram of the forces acting on the right cylinder is shown in Figure 13.

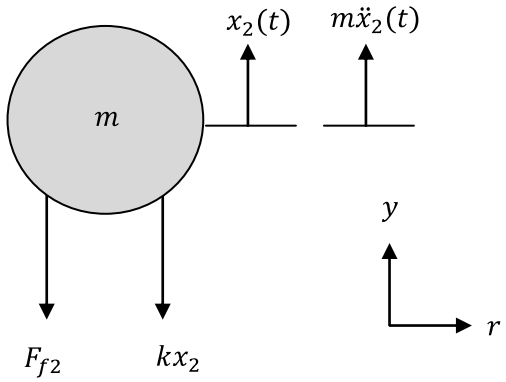

Figure 13 – Free body diagram for the right cylinder.

F_{f2}, is the fluid force acting on the right cylinder. The equation of motion for the right cylinder is

$$m\ddot{x}_2 = -kx_2 - F_{f2}. \tag{28}$$

The fluid force, $F_f(\omega)$, acting on a single oscillating infinite cylinder immersed in an unlimited mass of fluid is given by $F_f = -M' U_0 e^{i\omega t} i\omega \Gamma(R_\omega)$,

see Appendix B for more details. The fluid force acting on an oscillating cylinder can be expressed as,

$$F_f = -\gamma\, u_{cyl} \tag{29}$$

where the viscous damping is

$$\gamma(\omega) = M' i\omega \Gamma(R_\omega), \tag{30}$$

and velocity of the cylinder is,

$$u_{cyl} = U_0 e^{i\omega t}. \tag{31}$$

The fluid force acting on the right cylinder is

$$F_{f2} = -\gamma\,(u_y - \dot{x}_2) \tag{32}$$

where the velocity of the flow field, $u_y = -u_\theta(r = s, t)$ for $\theta = \pi/2$. The velocity $u_y - \dot{x}_2$ is relative to the right cylinder. The equation of motion is

$$\ddot{x}_2 - \gamma'\,\dot{x}_2 + \omega_0^2\, x_2 = -\gamma'\, u_y \tag{33}$$

where the natural frequency is given by ${\omega_n}^2 = k/m$, and the mass normalized viscous damping is $\gamma' = \gamma/m$. Eq. (33) is a linear second-order differential equation. We solve this using the Fourier transforms. We define the transform pair as,

$$\hat{x}(\omega) = \frac{1}{2\,\pi}\int_{-\infty}^{\infty} x(t)e^{-i\omega t}\,dt, \tag{34}$$

$$x(t) = \int_{-\infty}^{\infty} \hat{x}(\omega)e^{i\omega t}\,d\omega. \tag{35}$$

Transforming into Fourier space Eq. (33) becomes

$$-\omega^2\hat{x} - i\omega\gamma'(\omega)\hat{x} + \omega_0^2\hat{x} = -\gamma'(\omega)\hat{u}_y\,. \tag{36}$$

Where u_y can be written as,

$$u_y = -u_\theta(r,t) = -\lambda(\omega_d)e^{i\omega_d t}$$

and

$$\lambda(\omega_d) = \left(\frac{A}{s^2} - \frac{B}{a}\sqrt{iR_{\omega_d}}K_1'\left[\frac{s}{a}\sqrt{iR_{\omega_d}}\right]\right). \tag{37}$$

The Fourier transform of u_y is

$$\hat{u}_y(\omega) = \frac{1}{2\,\pi}\int_{-\infty}^{\infty} u_y e^{-i\omega t}\,dt = \frac{-1}{2\,\pi}\int_{-\infty}^{\infty} -\lambda(\omega_d)e^{-i\omega_d t}e^{-i\omega t}\,dt \tag{38}$$

which yields

$$\hat{u}_y(\omega) = -\lambda(\omega_d)\delta(\omega_d - \omega) \tag{39}$$

where δ is the Dirac delta function. The solution for $\hat{x}(\omega)$ is

$$\hat{x}(\omega) = \frac{-\gamma'(\omega_d)\hat{u}_y(\omega)}{-\omega^2 - i\omega\gamma'(\omega) + \omega_0^2} \tag{40}$$

where ω_d is the left cylinder's driving frequency. Assuming that the right cylinder's frequency is equal to the left cylinder's (i.e. $\omega_d = \omega$), Eq. (39) simplifies to

$$\hat{x}(\omega_d) = \frac{\gamma'\lambda(\omega_d)}{-{\omega_d}^2 - i\omega_d\gamma'(\omega_d) + \omega_0^2} \tag{41}$$

where

$$\gamma' = \frac{\gamma}{m} = T_0 i\omega\Gamma\left(R_{\omega_d}\right) \tag{42}$$

to yield

$$\hat{x}(\omega_d) = \frac{T_0 i\omega_d\Gamma\left(R_{\omega_d}\right)\lambda(\omega_d)}{{\omega_d}^2(T_0\Gamma\left(R_{\omega_d}\right) - 1) + \omega_0^2}. \tag{43}$$

If the right cylinder is driven at its resonance frequency (i.e. $\omega_0 = \omega_d$); this simplifies to

$$\hat{x}(\omega_d) = \frac{-\lambda(\omega_d)}{\omega_d} = \frac{-1}{\omega_d}\left(\frac{A}{s^2} - \frac{B}{a}\sqrt{iR_{\omega_d}}K_1'\left[\frac{s}{a}\sqrt{iR_{\omega_d}}\right]\right). \tag{44}$$

The right cylinder's displacement will be of the form

$$x_2(t) = A_{0_2}\sin(\omega_d t + \varphi). \tag{45}$$

The amplitude of oscillation for the right cylinder is given by,

$$A_{0_2} = [\hat{x}(\omega_d)\,\hat{x}^*(\omega_d)]^{1/2} \tag{46}$$

where the * represents the complex conjugate. The phase of oscillation with respect to the driving cylinder is given by

$$\varphi = \tan^{-1}\left(\frac{Im(\hat{x}(\omega_d))}{Re(\hat{x}(\omega_d))}\right). \tag{47}$$

The effects of the driven cylinder on a adjacent cylinder in terms of the amplitude, A_{02}, and the phase, φ, are illustrated in Figures 14 and 15 for a range of frequency based Reynolds number R_ω with specific values given in Table 3.

Table 3 - The five different frequency based Reynolds number explored.

R_ω	0.026	1	10	38	100

Figure 14 illustrates that the amplitude of oscillation decays quadratically as the normalized separation, s/a, increases, as expected from Eq. 44. As R_ω decreases the amplitude of oscillation for the right cylinder increases. This is because viscous forces increase with decreasing R_ω. Similarly, as R_ω decreases the Stokes length increases as ${R_\omega}^{-1/2}$.

Figure 15 shows that for $R_\omega \lesssim 10$ the phase of oscillation with respect to the driving cylinder is nearly constant and out of phase by ~ 2.8 radians (160^o) as the normalized separation, s/a, increases. For $R_\omega \lesssim 1$ an interesting phase variation occurs due to the fact that ${R_\omega}^{-1/2}$ is increasing making the flow dominated by viscous effects. Therefore for $R_\omega \lesssim 1$ the fluid coupling can be controlled by the varying normalized separation, s/a.

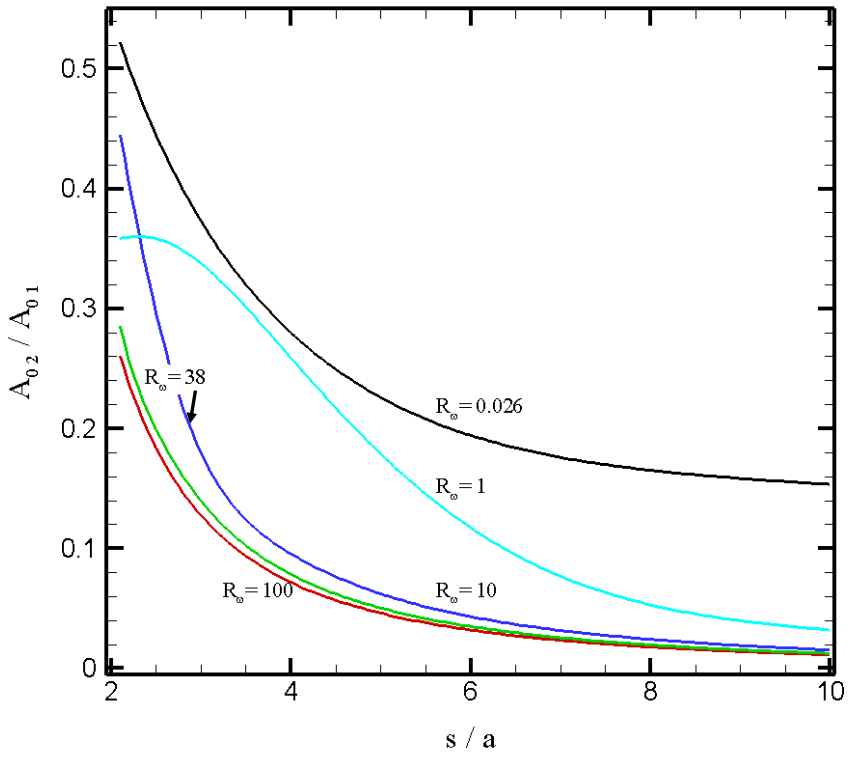

Figure 14 - The amplitude of oscillation, Eq. (46), for a range of frequency based Reynolds number R_ω. (Left axis) Normalized amplitude of oscillation of the right cylinder, A_{02},with amplitude of oscillation of the left cylinder A_{01}. (Bottom axis) Normalized separation.

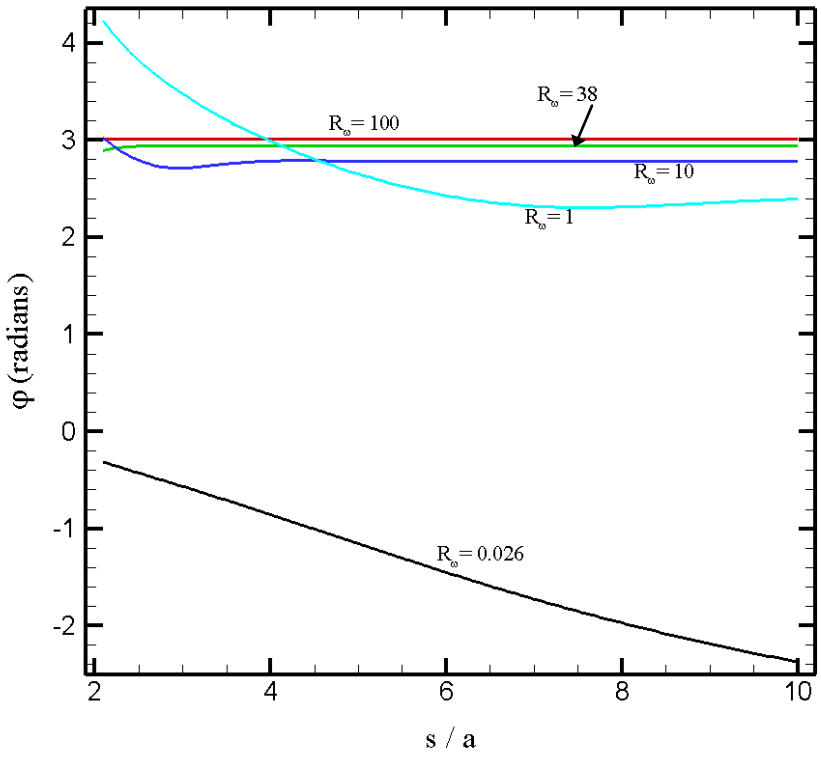

Figure 15 - The phase of oscillation, Eq. (47), for a range of frequency based Reynolds number R_ω. (Left axis) Normalized amplitude of oscillation of the right cylinder, A_{02}, with amplitude of oscillation of the left cylinder A_{01}. (Bottom axis) Normalized separation.

6 A numerical investigation of an array of cantilevers in fluid

In order to validate the analytical expressions developed and the assumptions we have made, full finite element numerical simulations are conducted of the fluid-coupled dynamics of an array of two infinite cylinders. We have simulated the time-dependent, three-dimensional, fluid solid interaction problem using the finite element solver CFD-ACE+ (31). The code solves the fluid dynamics utilizing a finite volume technique with first order Euler differencing in time that is coupled to a structural solver utilizing a finite element technique (32). This technique uses a pressure-based method to solve the incompressible Navier-Stokes equations. The fluid-structure interaction is coupled through the no-slip assumption so that the velocity of the fluid and solid mesh are equal at the interfaces.

6.1 Size of the numerical domain

In order to determine the size of the fluid domain where wall effects are negligible a series of tests were conducted using a single cylinder. The domain size was increased until the flow field far from the cylinder approached zero at the walls in a smooth manner.

Numerical results illustrated in Figure 24 show that the domain should be at least $21a$ to $27a$ away from the cylinder to be able to neglect wall effects. This is approximately 125 δ_s/a. In general, as the R_ω decreases the domain size increases, therefore increasing the number of Stokes lengths is required. The details of this validation are given in Appendix C. The normalized spatial-resolution chosen is $\Delta x/a = 0.34$ and the normalized time-resolution is $\Delta t/T = 0.05$. The simulations were conducted on a 3.2 GHz Xeon processor with 4GB of DDR memory. For a single cylinder oscillating in a viscous fluid, it takes approximately 3 hours to run a 200 time step simulation to obtain the steady oscillating solution.

6.2 Validation of results

It is important to validate the analytical predictions with the numerical simulations in order to verify the accuracy of the derived expressions. The two cylinders are separated by a distance s/a with specific values given in Table 4.

Table 4 - The ten different cylinder separations explored numerically.

s/a	2.2	2.3	2.4	2.5	3	3.5	4	6	8	10

Figure 16 shows that the analytics predicts higher amplitudes than the numerics. As the separation increases the analytics and numerics show good agreement. A reason that the analytics predicts higher amplitudes is because Eq. 44 does not include the back action of the adjacent cylinder on the driven cylinder. Moreover, the numerical solution solves the full Navier-Stokes equations. Lastly, it is important to recall that $R_u = 0.38$, which implies that the convective nonlinearity has a small contribution not captured by the analytics, therefore the analytics predicts higher amplitudes.

As expected from Eq. 44, the amplitude of oscillation decays quadratically as shown in Figure 17, where the numerical results yield $A_{02}(s) \sim s^{-2.06}$, and the theoretical results yield $A_{02}(s) \sim s^{-2}$.

Figures 18-20 illustrate a comparison between a single cylinder flow field and the flow field of two cylinders for numerics and theory for s/a = 2.5, 4, and 8. The two cylinder theory is the superposition of the flow field caused by each cylinder. The two cylinder theory is predicting higher fluid velocities produced by the right cylinder. This is expected because the analytics are predicting higher amplitudes in comparison with the numerics as shown in Figure 16. Also, the back action caused by the adjacent cylinder is not captured by the

analytics in comparison with the numerics, which can be illustrated in the flow field profile between the two cylinders. Again we note that $R_u = 0.38$, which implies that the convective nonlinearity has a small contribution not captured by the theory. Moreover, for large distances of separation, the flow field is similar to that for a single cylinder as expected.

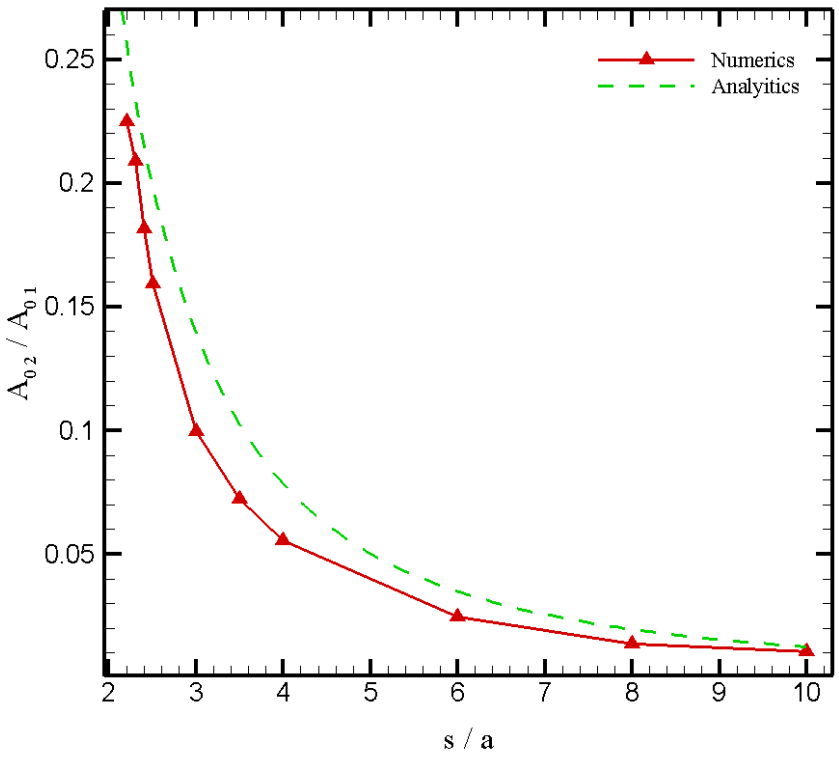

Figure 16 - Comparison between the analytics Eq. (46) and the numerical simulation for the amplitude of oscillation: (Dashed Line) analytics; (Solid Line) numerics. (Left axis) Normalized amplitude of oscillation of the right cylinder, A_{02},with amplitude of oscillation of the left cylinder A_{01}. (Bottom axis) Normalized separation.

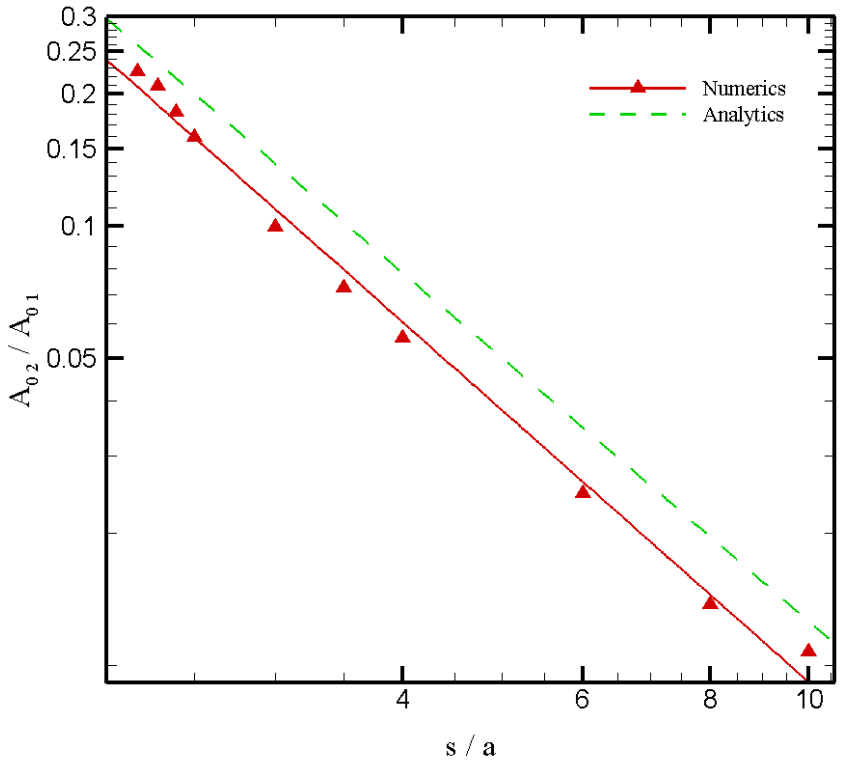

Figure 17 - Analytical and numerical data fitted with a power-law; (dashed line) analytics; (solid line) numerics. (Left axis) Normalized amplitude of oscillation of the right cylinder, A_{02},with amplitude of oscillation of the left cylinder A_{01}. (Bottom axis) Normalized separation.

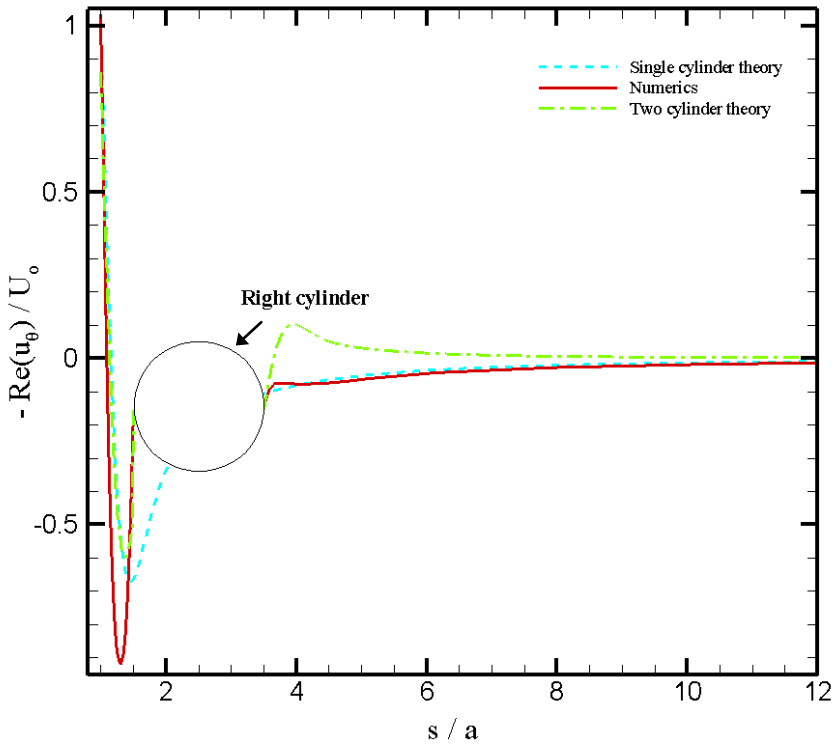

Figure 18 - Comparison between a single cylinder flow field and the flow field of two cylinders for s/a = 2.5; (Dashed Line) Single cylinder theory; (Solid Line) numerics; (DashedDot Line) Two cylinder theory. (Left axis) Normalized real part of the flow field velocity with the maximum velocity U_0. (Bottom axis) Normalized separation.

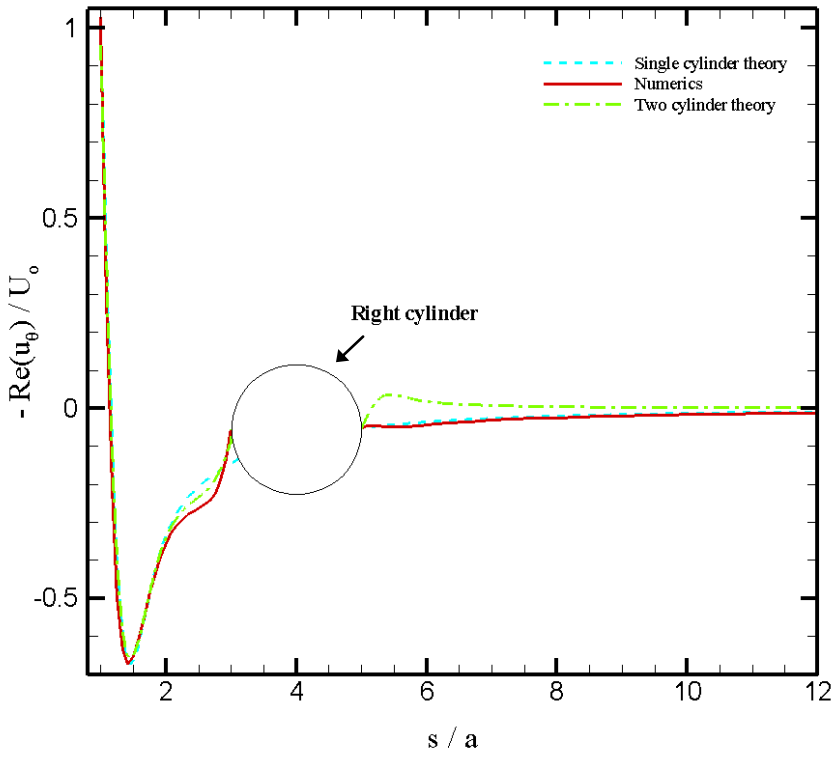

Figure 19 - Comparison between a single cylinder flow field and the flow field of two cylinders for s/a = 4; (Dashed Line) Single cylinder theory; (Solid Line) numerics; (DashedDot Line) Two cylinder theory. (Left axis) Normalized real part of the flow field velocity with the maximum velocity U_0. (Bottom axis) Normalized separation.

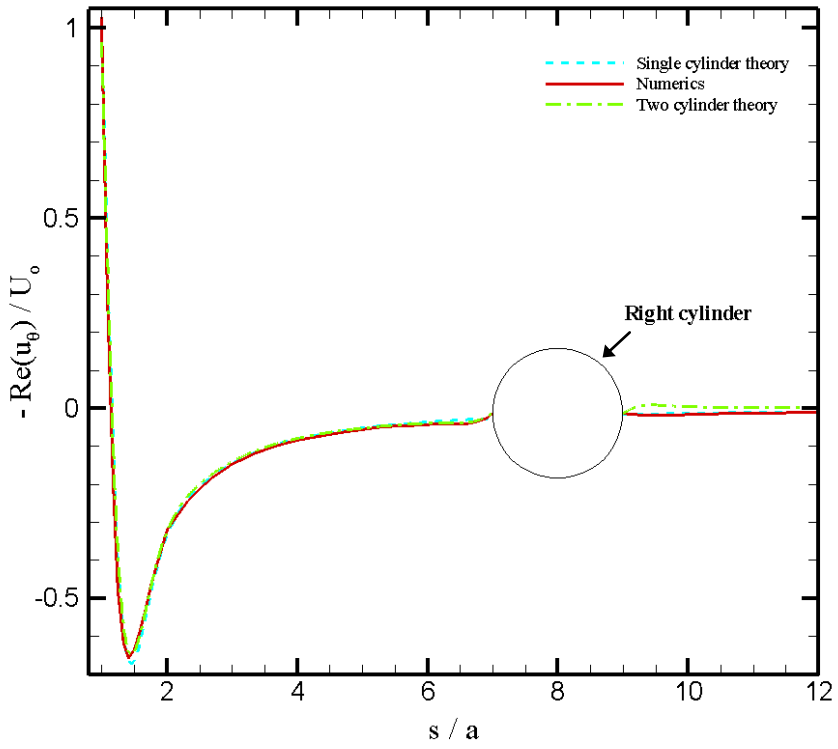

Figure 20 - Comparison between a single cylinder flow field and the flow field of two cylinders for s/a = 8. ; (Dashed Line) Single cylinder theory; (Solid Line) numerics; (DashedDot Line) Two cylinder theory. (Left axis) Normalized real part of the flow field velocity with the maximum velocity U_0. (Bottom axis) Normalized separation.

Figure 16 shows that analytics predicts a higher amplitude in comparison with the numerics. Therefore, it is expected that the fluid force acting on the right cylinder, F_{f2}, predicted by analytics is less than the one calculated by numerics as shown in Figure 21. Again this is due to the effect of numerical damping from the numerical solutions and the back action effect not captured by the analytics.

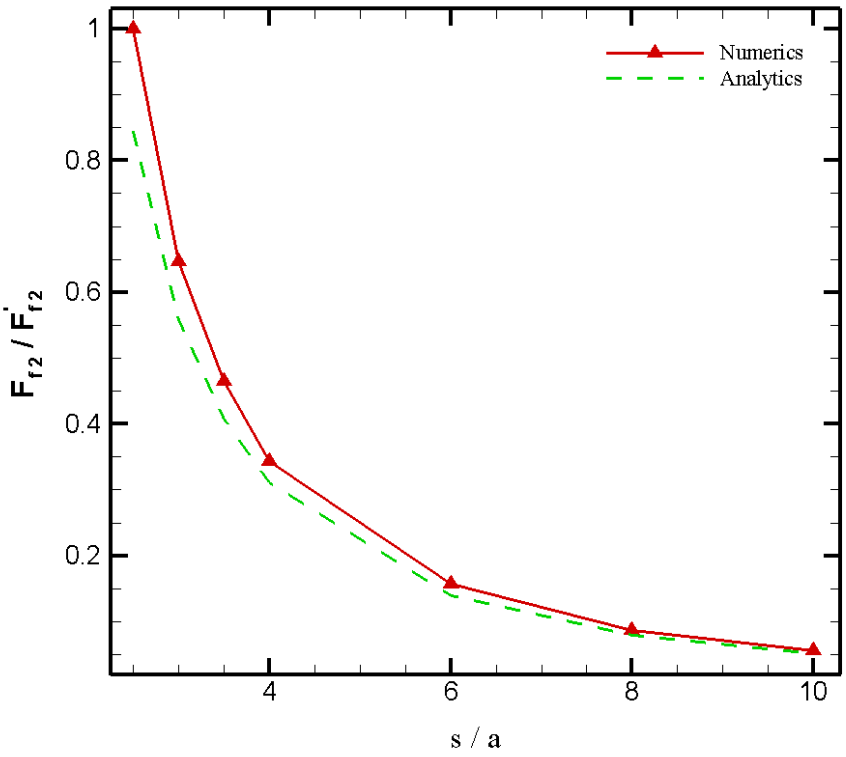

Figure 21 - Comparison between the analytics and the numerics. (Dashed Line) Results based upon the analytics for $F_{f\ 2}$. (Solid Line) Results from the numerical simulation for $F_{f\ 2}$. (Left axis) Normalized real part of the force of the right cylinder with the maximum force calculated from numerics $F'_{f\ 2}$. (Bottom axis) Normalized separation.

A comparison between analytics and numerics for the phase of oscillation is shown in Figure 22.

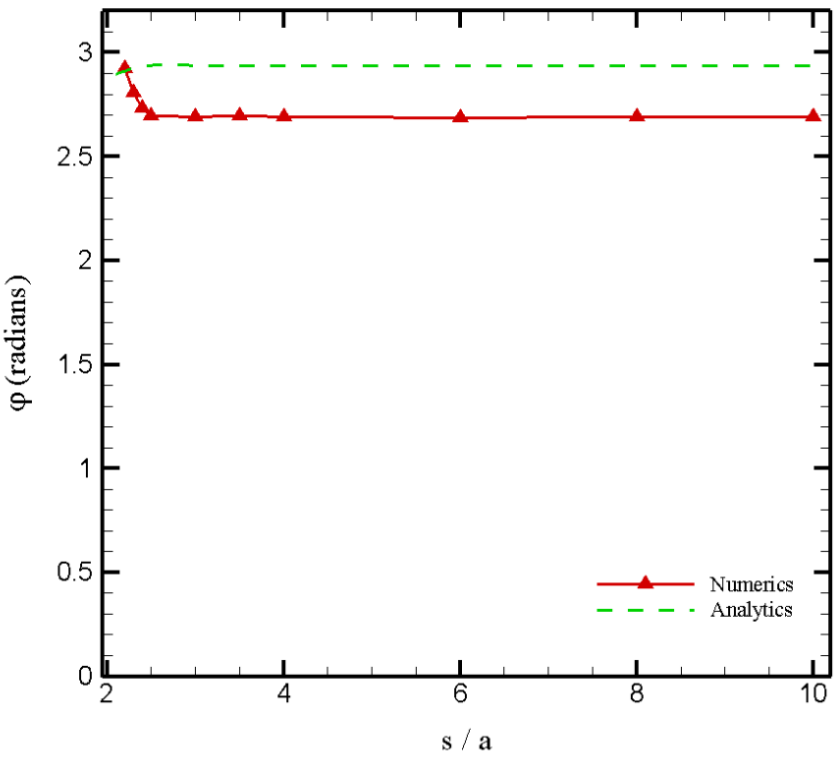

Figure 22 - Comparison of the analytics Eq. (45) and numerical predictions of the phase φ: (Dashed Line) analytics; (Solid Line) numerics. (Left axis) The phase of oscillation for the right cylinder (rad). (Bottom axis) Normalized separation.

Figure 22 shows that the displacement of the right cylinder is nearly out of phase with the left cylinder by ~ 2.8 radians (160^o) for the case studied. Since δ_s/a is small in comparison to the cylinder radius a, it is expected that the right cylinder is driven by pressure for larger separations therefore causing the right cylinder to be completely out of phase by π with the left cylinder. Again this is not captured here due to the effect of numerical damping from the numerical solutions and the back action effect is not captured by the analytics.

7 Conclusion

The dynamics of a single cantilever immersed in fluid that is driven to oscillate by means of a piezoshaker method was studied. It was shown that this method is promising for micro scale systems. Furthermore, the fluid-coupled dynamics of an array of two cantilevers immersed in fluid was considered. One cantilever was driven externally and the adjacent cantilever oscillated because of the resulting fluid motion. An analytical expression was developed for the amplitude and phase of a fluid-coupled cantilever. Full finite-element numerical simulations of the fluid-solid interactions for the precise geometries of interest were performed in order to validate the analytical expression. It was shown that the amplitude decays quadratically with increasing separation and that the fluid-coupled cantilever is nearly out of phase for any separation. The analytical expression provides important insight into analyzing and designing future micro and nanoscale technologies that are immersed in viscous fluids.

Appendix A

Derivation of the analytical solution for the flow field caused by an oscillating cylinder in fluid studied by Stokes in 1850 (28)(33). The unsteady Stokes equations are given by

$$\rho_f \frac{\partial \vec{u}}{\partial t} = -\vec{\nabla} p + \mu \nabla^2 \vec{u} \tag{A.1}$$

$$\vec{\nabla} \cdot \vec{u} = 0. \tag{A.2}$$

The x-momentum and the y-momentum equations for a Cartesian coordinate system are

$$\rho \frac{\partial u}{\partial t} = -\frac{\partial p}{\partial x} + \mu \left(\frac{\partial^2 u}{\partial x^2} + \frac{\partial^2 u}{\partial y^2} \right),$$

$$\rho \frac{\partial v}{\partial t} = -\frac{\partial p}{\partial y} + \mu \left(\frac{\partial^2 v}{\partial x^2} + \frac{\partial^2 v}{\partial y^2} \right). \tag{A.3}$$

The pressure gradient term ,$-\vec{\nabla} p$, can be eliminated by taking the partial derivative the of the x-momentum and y-momentum with respect to y and x, repectively and by subtracting both equations as follows,

$$\frac{\partial}{\partial y} \left[\rho \frac{\partial u}{\partial t} = -\frac{\partial p}{\partial x} + \mu \left(\frac{\partial^2 u}{\partial x^2} + \frac{\partial^2 u}{\partial y^2} \right) \right]$$

$$- \left(\frac{\partial}{\partial x} \left[\rho \frac{\partial v}{\partial t} = -\frac{\partial p}{\partial y} + \mu \left(\frac{\partial^2 v}{\partial x^2} + \frac{\partial^2 v}{\partial y^2} \right) \right] \right) \tag{A.4}$$

yielding,

$$\rho \frac{\partial}{\partial t} \left(\frac{\partial u}{\partial y} - \frac{\partial v}{\partial x} \right) = \mu \left[\frac{\partial}{\partial y} \left(\frac{\partial^2 u}{\partial x^2} \right) + \frac{\partial}{\partial y} \left(\frac{\partial^2 u}{\partial y^2} \right) - \frac{\partial}{\partial x} \left(\frac{\partial^2 v}{\partial x^2} \right) - \frac{\partial}{\partial x} \left(\frac{\partial^2 v}{\partial y^2} \right) \right]. \tag{A.5}$$

Using a stream function, ψ, where $u = \partial\psi/\partial y$ and $v = -\partial\psi/\partial x$ this becomes

$$\rho \frac{\partial}{\partial t}\left(\frac{\partial^2 \psi}{\partial x^2}+\frac{\partial^2 \psi}{\partial y^2}\right)=\mu\left[\frac{\partial^4 \psi}{\partial x^4}+\frac{2\,\partial^4 \psi}{\partial x^2 \partial y^2}+\frac{\partial^4 \psi}{\partial y^4}\right]. \tag{A.6}$$

Using

$$\nabla^2 \psi=\frac{\partial^2 \psi}{\partial x^2}+\frac{\partial^2 \psi}{\partial y^2} \quad \text{and} \quad \nabla^4 \psi=\frac{\partial^4 \psi}{\partial x^4}+\frac{2\,\partial^4 \psi}{\partial x^2 \partial y^2}+\frac{\partial^4 \psi}{\partial y^4}$$

Eq. (A.6) becomes

$$\left(\nabla^2-\frac{1}{\nu}\frac{\partial}{\partial t}\right)\nabla^2 \psi=0\,. \tag{A.7}$$

Eq. (A.7) represents the governing equation of the fluid motion in terms of the stream function. Eq. (A.7) is satisfied by $\psi=\psi_1+\psi_2$, where

$$\nabla^2 \psi_1=0 \tag{A.8}$$

$$\left(\nabla^2-\frac{1}{\nu}\frac{\partial}{\partial t}\right)\psi_2=0 \tag{A.9}$$

Notice that ψ_1 represents the potential part of the flow field and ψ_2 the represents the viscous part of the flow field. Closer to the oscillating cylinder, both components will contribute, but further away from the cylinder the flow field will only be potential. The solutions to Eq. (A.9) are

$$\psi_1=F_1(r)e^{i\omega t}\sin\theta \tag{A.10}$$

$$\psi_2=F_2(r)e^{i\omega t}\sin\theta \tag{A.11}$$

where

$$F_1(r)=\frac{A}{r} \tag{A.12}$$

$$F_2(r)=BK_1\left[\frac{r}{a}\sqrt{i\,R_\omega}\right] \tag{A.13}$$

K_1 is the modified Bessel function of the second kind and ψ can be written as

$$\psi = \left(\frac{A}{r} + BK_1\left[\frac{r}{a}\sqrt{i\,R_\omega}\right]\right)e^{i\omega t}\sin\theta. \tag{A.14}$$

In cylindrical coordinates the components of the fluid velocity field is $u_r = r^{-1}\partial\psi/\partial\theta$ and $u_\theta = -\partial\psi/\partial r$, where u_r represents the radial velocity and u_θ represents the angular velocity. By means of Eq. (A.14), the resulting flow field for a cylinder of radius a is given by,

$$u_r(r,t,\theta) = \frac{1}{r}\left(\frac{A}{r} + B\sqrt{iR_\omega}K_1\left[\frac{r}{a}\sqrt{iR_\omega}\right]\right)e^{i\omega t}\cos\theta \tag{A.15}$$

$$u_\theta(r,t,\theta) = \left(\frac{A}{r^2} - \frac{B}{a}\sqrt{iR_\omega}K_1'\left[\frac{r}{a}\sqrt{iR_\omega}\right]\right)e^{i\omega t}\sin\theta \tag{A.16}$$

and K_1' is the derivative of K_1. The constants A and B are found from the boundary conditions on the cylinder, where $u_r(r=a,t,\theta) = U_0\cos(\omega_f t)$ and $u_\theta(r=a,t,\theta) = -U_0\cos(\omega_f t)$, which gives

$$A = a^2U_0\left(1 - \frac{2K_1\sqrt{i\,R_\omega}}{K_1\sqrt{i\,R_\omega}+\sqrt{iR_\omega}K_1'\sqrt{i\,R_\omega}}\right), \tag{A.17}$$

$$B = \frac{2aU_0}{K_1\sqrt{i\,R_\omega}+\sqrt{iR_\omega}K_1'\sqrt{i\,R_\omega}}. \tag{A.18}$$

Appendix B

The fluid force, F_f, acting on an infinite cylinder. This was also studied by Stokes in 1850. The force is given by,

$$F_f = al \int_0^{2\pi} (T_{rr} \cos\theta - T_{r\theta} \sin\theta)\, d\theta \tag{B.1}$$

where T_{rr} and $T_{r\theta}$ are components of the stress tensor, which are defined as

$$T_{rr} = -p + 2\mu \frac{\partial u_r}{\partial r}, \tag{B.2}$$

$$T_{r\theta} = 2\mu \left[r \frac{\partial}{\partial r}\left(\frac{u_\theta}{r}\right) + \frac{1}{r}\frac{\partial u_r}{\partial \theta} \right]. \tag{B.3}$$

Eq. (B.1) can also be expressed using the stream function,

$$F_f = aL \int_0^{2\pi} \left(-p\ \cos\theta + \rho_f \frac{\partial \psi_2}{\partial t} \sin\theta \right) d\theta \tag{B.4}$$

the first term of Eq. (B.4) can be simplified using the product rule of differentiation, which can be integrated by parts as

$$\int_0^{2\pi} -p\ \cos\theta\ d\theta = p\ \sin\theta - \int_0^{2\pi} \left(\frac{dp}{\partial\theta}\right) \sin\theta\ d\theta \tag{B.5}$$

where

$$dp = \rho_f \frac{\partial}{\partial t}\left(\frac{\partial \psi_1}{\partial r} a\, d\theta - \frac{\partial \psi_1}{r \partial \theta} dr \right). \tag{B.6}$$

Notice that the first term of Eq. (B.5) vanishes at both limits by substituting Eq. (B.6) into the remainder of Eq. (B.5) and using Eq. (B.4). The force can be expressed as

$$F_f = -\rho_f al\ \frac{\partial}{\partial t} \int_0^{2\pi} \left\{ \left(\frac{\partial \psi_1}{\partial r} \right) a + \psi_2 \right\} \sin\theta\, d\theta. \tag{B.7}$$

Using the definitions of ψ_1, ψ_2, and integrating this becomes

$$F_f = -M' U_0 e^{i\omega t} i\omega \Gamma(R_\omega) \tag{B.8}$$

where $M' = \pi a^2 \rho_f$ is the mass per unit length of the fluid displaced by the cylinder and $\Gamma(R_\omega)$ is the hydrodynamic function,

$$\Gamma(R_\omega) = 1 - \frac{4K_1\sqrt{i\,R_\omega}}{K_1\sqrt{i\,R_\omega}+\sqrt{iR_\omega}K_1'\sqrt{i\,R_\omega}}. \tag{B.9}$$

Appendix C

A spatial-resolution (Δx) and time-resolution (Δt) study of the finite-element numerical procedure was conducted for the values used are shown in Table 5.

Table 5 - Values of spatial, Δx, and temporal, Δt, discretization used in the convergence study, where a is the cylinder radius and T is the period of oscillation, $T = 2\pi/\omega_f$.

Spatial-resolution study		Time-resolution study	
$\Delta x/a$	$\Delta t/T$	$\Delta x/a$	$\Delta t/T$
0.14	0.05	0.14	0.05
0.2	0.05	0.14	0.025
0.28	0.05	0.14	0.0125
0.34	0.05	0.14	0.00625

The error E was calculated by comparing the numerical flow fluid u with the exact analytical solution u_e given by Eq. (11) using

$$E = \frac{1}{N}\sum_{i=1}^{N} | u - u_e | \tag{C.1}$$

where N is the number of data points . The error as a function of spatial and time resolution is shown in Figure 23.

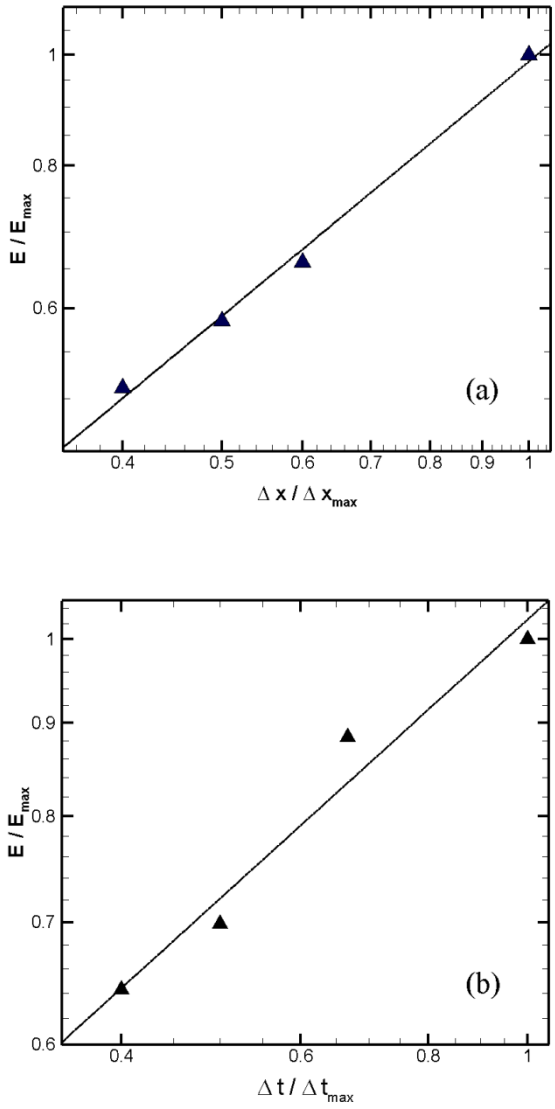

Figure 23 - Panel (a), the error as a function of spatial-resolution. (Left axis) Normalized absolute error with the maximum absolute error E_{max}. (Bottom axis) Normalized spatial resolution Δx with the maximum spatial-resolution Δx_{max}. Panel (b), the error as a function of time-resolution. (Left axis) Normalized absolute error with the maximum absolute error E_{max}. (Bottom axis) Normalized time-step Δt with the maximum time-step Δt_{max}.

A power-law fit to the data yields $E(\Delta x) \approx \Delta x^{0.74}$ and $E(\Delta t) \approx \Delta t^{0.51}$. The slopes of the power fitted curves are ~1, which implies that the simulations are approximately first order accurate. For the time resolution we expected the slope to be linear because the time accuracy used for the simulation is first order Euler. For the spatial resolution we expected the slope to be linear because the stress solver is first order elements by default. This implies that the convergence of the error is not decreasing as expected, therefore making the numerical calculations converge slower. Considering these results, it was decided to use $\Delta x/a = 0.34$ and $\Delta t/T = 0.05$, in the following studies. A comparison between the numerical solution and the analytical expression given by Eq. (11) is illustrated in Figure 24.

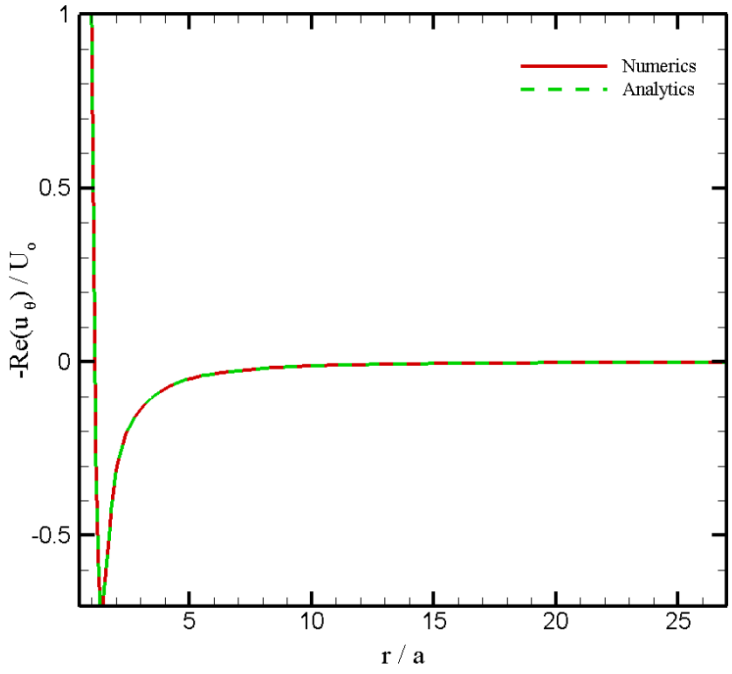

Figure 24 - Comparison between analytics given by Eq. (11) and the numerical simulation: For u_θ (r, $\theta = \pi/2$) (dashed line) analytics; (solid line) numerics. (Left axis) Normalized real part of the flow field velocity with the maximum velocity of the cylinder U_0. (Bottom axis) Normalized radial distance, where *a* is the cylinder radius.

The fluid force, F_f, is compared with analytical results given by Eq. (18) illustrated in Figure 25.

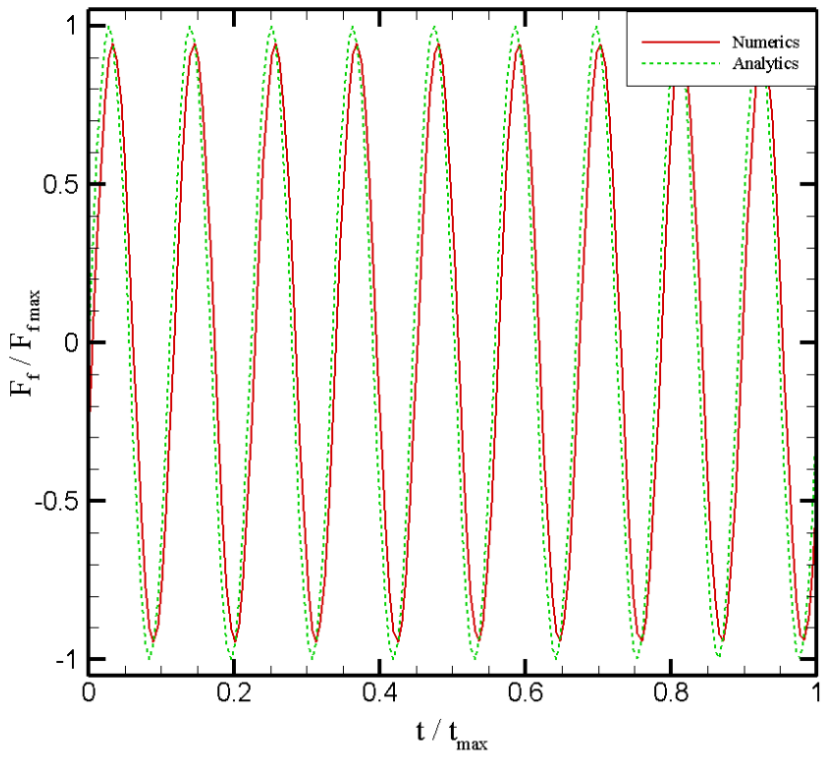

Figure 25 - Comparison between the analytics given by Eq. (18) and the numerical simulation; (dashed line) analytics; (solid line) numerics. (Left axis) Normalized force with the maximum force F_{fmax}. (Bottom axis) Normalized time t with the maximum time t_{max}.

Figure 25 shows that the force from the numerical simulation is slightly out of phase with the analytical prediction. This deviation can be reduced by decreasing the time step. However, we have found that the increased computational cost is prohibitive.

List of References

1. Feyman R P. *There is plenty of room at the bottom.* Journal of Microelectromechanical Systems, 1992. pp. 60-66. Vol. 1.

2. Feynman R P. *Infinitesimal Machinery.* Journal of Microelectromechanical Systems, 1993. pp. 4-14. Vol. 2.

3. Binnig G, Quate C F and Gerber C. *Atomic force microscope.* Physical Review Letters, 1986. pp. 930-933. Vol. 56.

4. Archibald R, Datskos P, Devault G, Lamberti V, Lavrik N, Noid D, Sepaniak M and Dutta P. *Independent component analysis of nanomechanical responses of cantilever arrays.* Analytica Chimica Acta, 2007. pp. 101-105. Vol. 584.

5. Bargatin I, Kozinsky I and Roukes M L. *Efficient electrothermal actuation of multiple modes of high-frequency nanoelectromechanical resonators.* Applied Physics Letters, 2007. Vol. 90.

6. Lavrik N V and Datskos P G. *Femtogram mass detection using photothermally actuated nanomechanical resonators.* Applied Physics Letters, 2003. pp. 2697-2699. Vol. 82.

7. Cleland A N and Roukes M L. *Fabrication of high frequency nanometer scale mechanical resonators form bulk Si crystals.* Applied Physics Letters, 1996. pp. 2653-2655. Vol. 69.

8. Verbridge S S, Bellan L M, Parpia J M and Craighead H G. *Optically driven resonance of nanoscale flexural oscillators in liquid.* Nano Letters, 2006. pp. 2109-2114. Vol. 6.

9. Rugar D, Budakian R, Mamin H J and Chui B W. *Single spin detection by magnetic resonance force microscopy.* Nature, 2004. pp. 329-332. Vol. 430.

10. Harley J A and Kenny T W. *High-sensitivity piezoresistive cantilevers under 1000 angstrom thick.* Applied Physics Letters, 1999. pp. 289-291. Vol. 75.

11. Bargatin I, Myers E B, Arlett J, Gudlewski B and Roukes M L. *Sensitive detection of nanomechanical motion using piezoresistive signal downmixing.* Applied Phyisics Letters, 2005. Vol. 86.

12. Li M, Tang H X and Roukes M L. *Ultra-sensitive NEMS- based cantilevers for sensing, scanned probe and very high-frequency.* Nature Nanotechnology, 2007. pp. 114-120. Vol. 2.

13. Arntz Y, Seelig J D, Lang H P, Zhang J, Hunziker P, Ramseyer J P, Meyer E, Hegner M and Gerber C. *Label-free protein assay based on a nanomechanical cantilever array.* Nanotechnology, 2003. pp. 86-90. Vol. 14.

14. McKendry R, Zhang J Y, Arntz Y, Strunz T, Hegner M, Lang H P, Baller M K, Certa U, Meyer E, Guntherodt H J and Gerber C. *Multiple label-free biodetection and quantitative DNA-binding assays on a nanomechanical cantilever array.* Proceedings of the National Academy of Science of the United States of America, 2002. pp. 9783-9788. Vol. 99.

15. Fritz J, Baller M K, Lang H P, Rothuizen H, Vettiger P, Meyer E, Guntherodt H J, Gerber C and Gimzewski J K. *Translating biomolecular recognition into nanomechanics.* Science, 2000. pp. 316-318. Vol. 288.

16. Hansen W R and Autumn K. *Evidence for self cleaning in gecko setae.* Proceedings of the National Academy of Science of the United States of America, 2005. pp. 385-389. Vol. 102.

17. Meiners J C and Quake S R. *Direct measurement of hydrodynamic cross correlations between two particles in an external potential.* Physical Review Letters, 1999. pp. 2211-2214. Vol. 82.

18. Meiners J C and Quake S R. *Femtonewton force spectroscopy of single extended DNA molecules.* Physical Review Letters, 2000. pp. 5014-5017. Vol. 84.

19. Tuck E O. *Calculation of unsteady flows due to small motions of cylinders in viscous fluid.* Journal of Engineering Mathematics, 1969. pp. 29-44. Vol. 3.

20. Sader J E. *Frequency response of cantilever beams immersed in viscous fluids with applications to the atomic force microscope.* Journal of Applied Physics, 1998. pp. 64-76. Vol. 84.

21. Basak S, Raman A and Garimella S V. *Hydrodynamic loading of microcantilevers vibrating in viscous fluids.* Journal of Applied Physics, 2006. p. Art. No. 114906. Vol. 99.

22. Basak S and Raman A. *Hydrodynamic coupling between micromechanical beams oscillating in viscous fluid.* Physics of Fluid, 2007. p. Art. No. 017105. Vol. 19.

23. Paul M R and Cross M C. *Stochastic dynamics of nanoscale mechanical oscillators immersed in a viscous fluid.* Physical Review Letters, 2004. Vol. 92.

24. Clark M T and Paul M R. *The stochastic dynamics of an array of atomic force microscopes in a viscous fluid.* Int. J. Non-Linear Mech, 2007. pp. 690-696. Vol. 42.

25. Atakhorrami M, Sulkowska J I, Addas K M, Koenderink G H, Tang J X, Levine A J, MacKintosh F C and Schmidt C F. *Correlated fluctuations of microparticles in viscoelastic solutions: Quantitative measurement of material properties by microrheology in the presence of optical traps.* Physical Review E, 2006. Vol. 73.

26. Chon J W M, Mulvaney P and Sader J E. *Experimental validation of theoretical models for the frequency response of atomic force microscope cantilever beams immersed in fluids.* Journal of Applied Physics, 2000. pp. 3978-3988. Vol. 87.

27. Darniadakis G, Beskok A and Aluru N. *Micro flows: fundamental and simulation.* New York : Springer, 2002.

28. Stokes G G. *On the effect of the internal friction of fluids on the motion of pendulums.* Transactions of the Cambridge Philosophical Society, 1850. pp. 1880-1905. Vol. 9.

29. Paul M R, Clark M T and Cross M C. *The stochastic dynamics of micron and nanoscale elastic cantilevers in fluid: flunctuations from dissipation.* Nanotechnology, 2006. pp. 4502-4513. Vol. 17.

30. Inman D J. *Engineering Vibration.* Upper Saddle River : Prentice-Hall, Inc., 2001.

31. *ESI Group Web site.* [Online] ESI Group. http://www.esi-group.com.

32. Yang H Q and Makhijani V B. *A strongly-coupled pressure-based CFD algorithm for fluid-structure interaction.* 32nd AIAA Aerospace sciences meeting & exhibit; Reno, NV, 1994. pp. 1-10.

33. Rosenhead L. *Laminar Boundary Layers.* Oxford : Clarendon Press, 1963.

Vita

Carlos Carvajal is from Colombia, South America and moved to Athens, Tennessee when he was sixteen years old. Carlos attended Tennessee Technological University in the fall of 2004. As the President of ASME student chapter, he won 1st place in the Old Guard Technical Poster Competition at the 2006 ASME District Regional Conference in Tampa, Florida. Carlos was also involved with Pi Tau Sigma student chapter where he was the Vice-President. Carlos gave back to Tech by participating in events on campus through the President's Ambassador Program. Carlos graduated from Tennessee Tech in the spring of 2006. After graduation, Carlos attended Virginia Tech as a Master's student under Dr. Mark Paul. Carlos will graduate in the fall of 2007 and will join Eastman Chemical Company as a mechanical engineer, but will return for more Hokie football action!